A critical period of translational control during brain development at codon resolution

Dermot Harnett,[1,9,*] Mateusz C. Ambrozkiewicz,[2,9,*] Ulrike Zinnall,[1] Alexandra Rusanova,[3] Ekaterina Borisova,[3] Rike Dannenberg,[2] Koshi Imami,[4,5] Agnieszka Münster-Wandowski,[6] Beatrix Fauler,[7] Thorsten Mielke,[7] Matthias Selbach,[5] Markus Landthaler,[1] Christian M.T. Spahn,[8] Victor Tarabykin,[2,3,†] Uwe Ohler,[1,†] Matthew L. Kraushar[7,†,*]

[1] Berlin Institute for Medical Systems Biology, Max Delbrück Center for Molecular Medicine, 10115 Berlin, Germany

[2] Institute of Cell Biology and Neurobiology, Charité-Universitätsmedizin Berlin, corporate member of Freie Universität Berlin, Humboldt-Universität zu Berlin, and Berlin Institute of Health, 10117 Berlin, Germany

[3] Institute of Neuroscience, Lobachevsky University of Nizhny Novgorod, pr. Gagarina 24, Nizhny Novgorod, Russian Federation

[4] Department of Molecular and Cellular BioAnalysis, Graduate School of Pharmaceutical Sciences, Kyoto University, Kyoto 606-8501, Japan

[5] Max Delbrück Center for Molecular Medicine, 13092 Berlin, Germany

[6] Institute of Neuroanatomy, Charité-Universitätsmedizin Berlin, 10117 Berlin, Germany

[7] Max Planck Institute for Molecular Genetics, 14195 Berlin, Germany

[8] Institute of Medical Physics and Biophysics, Charité-Universitätsmedizin Berlin, 10117 Berlin, Germany

[9] These authors contributed equally

[†] Senior author

*Correspondence:
dermot.harnett@mdc-berlin.de (D.H.);
mateusz-cyryl.ambrozkiewicz@charite.de (M.C.A.);
matthew.kraushar@molgen.mpg.de (M.L.K.)

SUMMARY

Translation modulates the timing and amplification of gene expression after transcription. Brain development requires uniquely complex gene expression patterns, but large-scale measurements of translation directly in the prenatal brain are lacking. We measure the reactants, synthesis, and products of translation spanning mouse neocortex neurogenesis, and discover a transient window of dynamic regulation at mid-gestation. Timed translation upregulation of chromatin binding proteins like Satb2, which are essential for neuronal subtype differentiation, restrict protein expression in neuronal lineages despite broad transcriptional priming in progenitors. In contrast, translation downregulation particularly impacts ribosomal proteins and sharply decreases ribosome number, shifting protein synthesis dynamics at mid-gestation. Changing levels of eIF4EBP1 – a direct inhibitor of ribosomal protein translation – coincides with ribosome downregulation, and controls Satb2 fate acquisition during neuronal differentiation. Thus, the refinement of transcriptional programs by translation is central to the molecular logic of brain development. The developmental neocortex translatome is provided open-source: https://shiny.mdc-berlin.de/cortexomics/.

INTRODUCTION

Changes in translation activity can lead to significant discrepancies between mRNA and protein for the same gene, and are a hallmark of many dynamic cellular transition states (Buccitelli and Selbach, 2020). Dynamic cellular transitions are uniquely complex during brain development from neural stem cells, which must deploy highly sophisticated gene expression programs (Cadwell et al., 2019; DeBoer et al., 2013). In evolutionarily advanced brain regions like the neocortex, a cell's transcriptional signature alone appears insufficient to account for the enormous cellular diversity, with recent single-cell RNA sequencing (scRNA-seq) analyses supporting this idea (Nowakowski et al., 2017; Telley et al., 2019; Zahr et al., 2018). While transcriptional profiles define broad classes of neurons and non-neuronal cells, a striking conclusion from these studies was the degree of homogeneity in mRNA pools across neuronal lineages during stem cell differentiation (Cadwell et al., 2019; Telley and Jabaudon, 2018). Thus, the blueprint of gene expression in evolutionarily advanced brain regions is likely a multilayered, progressive refinement – including and beyond transcription (Cadwell et al., 2019). Neocortex development may thus represent a particularly dynamic cellular system of translational control. (Hoye and Silver, 2021; Kraushar et al., 2016).

Direct measurements of protein synthesis would provide a clearer picture of functional gene expression in the developing brain; however, a large-scale high-resolution analysis of mRNA translation during neurogenesis has lagged behind transcriptome analysis, in part due to current technical limitations in protein measurement. Recent work suggests that targeted and selective protein synthesis refines the output of gene expression in brain development (Kraushar et al., 2014, 2015, 2021; Popovitchenko et al., 2020; Zahr et al., 2018, 2019). Importantly, abnormal ribosome levels and disrupted translation was found recently to be a mid-gestation etiology of neurodevelopmental disorders (Kalish et al., 2021). However, how ribosomes decode mRNA in the transcriptome-to-proteome transition during developmental neurogenesis remains unknown.

To circumvent these challenges and measure the temporal dynamics of the reactants, synthesis, and products of mRNA translation during brain development, we performed sequencing of ribosome-protected mRNA fragments (Ribo-seq; ribosome profiling) (Ingolia et al., 2009) in parallel with RNA-seq, tRNA qPCR array, and mass spectrometry across five stages of mouse neocortex neurogenesis. By capturing ribosome-mRNA interactions at codon-

level resolution, we find that ~ 18 % of mRNAs change translation efficiency in the progressive specification of neural stem cells to post-mitotic neurons, with a transient peak window of dynamic translation at mid-gestation.

Divergent cellular pathways are impacted by translation upregulation vs. downregulation during neurogenesis. Chromatin binding proteins like *Satb2*, essential for the differentiation of neuronal subtypes (Britanova et al., 2008), are the most translationally upregulated mRNAs. We find *Satb2* mRNA is transcribed unexpectedly broadly in neuronal lineages, but achieves restricted neuronal subtype-specific protein expression by timed translation. In contrast, ribosomal proteins are the most translationally downregulated, coinciding with dynamic expression of eIF4EBP1, a translational repressor targeting these transcripts directly (Jin et al., 2020; Thoreen et al., 2012). An acute decrease in ribosome number leads to widespread changes in global translation kinetics at mid-gestation – a critical period for neurodevelopmental pathology (Kalish et al., 2021). Finally, *in utero* knockdown of eIF4EBP1 in neural progenitors to disrupt the balance of translation during this window leads to decreased specification of the Satb2 neuronal lineage and migration arrest.

Thus, by mapping the quantitative landscape of the transcriptome-to-proteome transition in the neocortex, we find that protein synthesis is a powerful and widespread layer of gene expression regulation that shifts kinetics and impacts neuronal specification during development. We provide the developmental neocortex translatome as an open-source searchable web resource: https://shiny.mdc-berlin.de/cortexomics/.

RESULTS

Deep sequencing of translation reveals a spike in regulation during neurodevelopment

We focused our study on the mammalian neocortex, an evolutionarily advanced and dynamic developmental system with a tightly timed sequence of neurogenesis (DeBoer et al., 2013; Greig et al., 2013) (**Figure 1A**). At embryonic day 12.5 (E12.5) this predominantly stem cell tissue gives birth to its first neurons. Neurons born early at E12.5 form distinct connections and control different functions than those born later at E15.5. By postnatal day 0 (P0), neurogenesis is largely complete. The timed sequence of gene expression is essential to specify neuronal fate from the stem cell pool.

We designed a strategy to analyze the major reactants, synthesis, and products of mRNA translation across five stages encompassing neocortex neurogenesis (**Figure 1A**), including Ribo-seq measurement of ribosome-mRNA interactions, in parallel with RNA-seq, tRNA qPCR array, and mass spectrometry. Ribo-seq measures 80S ribosomes bound to the open reading frame of mRNA – a quantitative indicator of active protein synthesis at codon-level resolution (Ingolia et al., 2009). Optimizations for analysis of neocortex ribosomes *ex vivo* circumvented the requirement for pharmacological ribosome stalling with cycloheximide (Kraushar et al., 2021), which introduces ribosome footprint redistribution artifacts (Ingolia, 2016), and enabled efficient nuclease digestion to generate high fidelity ribosome-protected mRNA fragments (RPFs) (**Figure S1**). Quantifying both RNA-seq and Ribo-seq in an isoform-aware fashion, we obtained transcripts per-million (TPM) and RPF densities for 22,373 genes (**Figure S2A, Table S1**). Reproducibility of both RNA and RPF measurements permitted reliable calculation of mRNA translation efficiency (**Figures S2B-D**), which represents the ratio between ribosome binding to an mRNA's coding sequence and the mRNA's level overall (**Figure 1B**). As a quality control, we focused further analysis on coding sequences with 32 or more Ribo-seq footprints in at least one stage as per (Dunn et al., 2013), which resulted in a set of 12,228 translated GENCODE-annotated transcripts.

To detect translation-specific gene expression regulation, we first calculated fold changes between sequential time points in mRNA or RPF vs. protein (**Figure 1C, Table S2**). While gene expression overall is quite stable between E12.5 and E14, a burst of regulation occurs at E15.5 at both transcriptional and translational levels, with a significant impact on the proteome. However, robust RPF fold changes persist until P0, with mRNA changes less pronounced. Strikingly, calculation of translation efficiency highlighted a transient window of robust regulation at E15.5, coinciding with a crucial transition in neuronal fate specification. Translation efficiency upregulation was found to occur in 1,129 genes and downregulation in 1,131 genes. A further 2,253 genes change in steady state mRNA only, without any significant translation efficiency change. Thus, we estimate ~ 18 % of the transcriptome is dynamically translated across neocortex neurogenesis, with an acute inflection point during the mid-neurogenesis transition at E15.5.

Our Ribo-seq data shows a higher correlation with protein levels than RNA-seq data, for both inter-gene comparisons within a sample (**Figure S3A**) and fold changes over time (**Figure 1C**).

We decomposed technical and systematic variation in protein levels, and estimated proportions explained by RNA-seq vs. Ribo-seq (Li et al., 2014) (**Figures 1D and S3B**). A majority of protein level variance is accounted for by RNAseq, in agreement with prior observations (Jovanovic et al., 2015; Li et al., 2014). However, Ribo-seq consistently explains a higher fraction of protein variation than RNA-seq at each developmental stage, especially for proteins with increasing levels as expected, given that Ribo-seq is a direct measurement of protein synthesis. The protein level predictivity of Ribo-seq was particularly pronounced for genes with changing translation efficiency.

Thus, our data enable detection of regulation that impacts the protein output of gene expression, which includes a transient window of robust translation control at E15.5.

Divergent trajectories of mRNA and protein reveal distinct developmental programs of translation

Gene expression trajectory over time is indicative of coordinated developmental programs, where deviations between mRNA and protein may represent dynamic cellular transitions (Buccitelli and Selbach, 2020). We next performed hierarchical clustering of mRNA and protein expression trajectories after E12.5 per gene, which divided the proteome into 13 broad clusters (**Figures 2A and S3C, Table S3**). We found clusters representing concordant and divergent trajectories between mRNA and protein, with E15.5 a common inflection point of divergent regulation. While genes with changing translation efficiency are found in all clusters, they are enriched in clusters that demonstrate highly divergent mRNA and protein expression. Furthermore, several essential neural stem cell and differentiation markers segregate into distinct clusters, such as *Nes* in cluster J and *Satb2* in cluster M. Reinforcing the biological significance of clusters representing different mRNA and protein trajectories, gene ontology analysis demonstrated many non-overlapping, distinct pathways enriched in different clusters, such as neuron differentiation processes enriched in cluster D (**Figure 2B, Table S3**).

The relationship between Ribo-seq densities and steady state protein levels is complicated by the fact that protein half-lives are relatively long (Schwanhäusser et al., 2011), and reflect the cumulative effects of synthesis and degradation over time. In contrast, Ribo-seq reflects synthesis at a given time point. Deviations between protein and Ribo-seq are expected whenever protein levels have not yet reached equilibrium with synthesis, making linear

comparison of protein concentrations and Ribo-seq densities difficult to interpret. We therefore made use of a kinetic, time continuous model of protein translation similar to (Becker et al., 2018) (see **Methods**).

We classified proteins into one of five categories (**Figure 2C**): *stationary*, where protein levels showed little change; *linear*, where protein levels were in near-equilibrium with Ribo-seq measured synthesis; *production*, consistent with a non-equilibrium protein trajectory; *degradation*, for which protein degradation alone fit the data; and *"MSdev"*, whose protein trajectories diverged from their Ribo-seq trajectory for any combination of parameters. Then, by using the approximation of single constant relating RPF density and synthesis rate, we were able to estimate half-lives for all genes, which show a strong correlation to experimentally determined degradation rates in NIH 3T3 cells (McShane et al., 2016) (**Figure S3D**). For example, our predicted MSdev category proteins are more likely to demonstrate non-exponential decay kinetics during their lifetime (**Figure S3E**).

Genes in the five modeled categories showed distinct gene ontology term enrichment (**Figure 2D**), such as the linear relationship between the synthesis and abundance of ribosome components, or the non-linear relationship for chromatin associated proteins. Interestingly, G-protein coupled receptors and DNA replication genes are enriched in the MSdev category, suggesting their expression patterns are highly multifaceted. In contrast, transmembrane transporter protein levels are highly stable, buffering any upstream gene expression patterns. Thus, our modeling highlights how multiple layers of post-transcriptional regulation impact distinct gene families during the time course of neuronal differentiation.

Translation upregulation of chromatin binding proteins like Satb2 establishes neuronal fate

We first focused on the cohort of genes that are translation efficiency upregulated across neurogenesis after E12.5, to identify essential neurodevelopmental proteins with dynamic translation. Gene ontology analysis demonstrated chromatin binding proteins are particularly subject to translation upregulation (**Figure 3A**). Chromatin binding proteins like transcription factors have a powerful influence on the neuronal fate of stem cells, which is tightly coordinated in developmental time. *Early*-born neurons ultimately express transcription factors like Bcl11b, which drives them to connect *sub*-cortically (Arlotta et al., 2005). In contrast, *late*-

181 born neurons after E15.5 ultimately express transcription factors like Satb2, which drives them
182 to connect *intra*-cortically (Alcamo et al., 2008; Britanova et al., 2008). How proteins like
183 transcription factors achieve neuronal subtype and temporally restricted expression is a critical
184 question.
185
186 Strikingly, among the most translationally upregulated neurodevelopmental proteins
187 discovered in our data is late-born upper layer neuron transcription factor Satb2 (**Figure 3B**).
188 We assessed the trajectory of Satb2 synthesis in our RNA-seq, Ribo-seq, and mass spec data
189 along with calculated translation efficiency; in comparison to the intermediate filament protein
190 Nes expressed by neural stem cells (Frederikson and McKay, 1988), and early-stage
191 transcription factor Bcl11b expressed in neurons positioned adjacent to the later Satb2 lineage.
192 As expected, Nes demonstrates predominantly transcriptionally driven expression
193 downregulation, as the neural stem cell pool is depleted by neuronal differentiation
194 (Josephson et al., 1998). Bcl11b is expressed in the early-born lineage with high concordance
195 between RNA-seq and Ribo-seq, and with low fluctuations in translation efficiency. In contrast,
196 fold changes in Satb2 Ribo-seq and MS signal are in excess of the RNA-seq, with 2-fold
197 translation efficiency upregulation reaching a plateau at E15.5. These data suggest that *Satb2*
198 expression is amplified by translation.
199
200 To test the hypothesis that *Satb2* mRNA undergoes translation regulation, we examined the
201 cellular distribution of *Satb2* mRNA in comparison to the protein expression in later born upper
202 layer neurons (Alcamo et al., 2008; Britanova et al., 2008). Analysis of scRNA-seq data (Telley
203 et al., 2019) revealed that *Satb2* mRNA is robustly expressed in differentiated neurons of both
204 the early- and late-born lineages (**Figure 3C**). Thus, transcription of this upper layer program
205 may occur in neuronal lineages that include lower layers, and outside of the expected protein
206 distribution.
207
208 To directly visualize the expression of *Satb2* mRNA and protein, we performed fluorescence *in*
209 *situ* hybridization and immunohistochemistry in neocortical coronal sections (**Figure 3D**), with
210 probe and antibody specificity confirmed in *Satb2*$^{-/-}$ brains (**Figure S4A**), and signal quantified
211 per cell (**Figures 3E and S4B, Table S4**). At the onset of neurogenesis E12.5, we detected
212 robust *Satb2* mRNA signal throughout the neocortex, from the ventricular zone in multipotent
213 progenitors and throughout the nascent cortical plate in early-born neurons. Satb2 protein was

214 undetectable at this stage, whereas weak Bcl11b protein signal matched its cortical plate-
215 localized mRNA signal. Notably, almost half of all *Satb2* mRNA clusters colocalize with *Bcl11b*
216 mRNA puncta in neurons differentiating in the cortical plate, but rarely in the stem cell niche of
217 the ventricular zone.
218
219 We first detected Satb2 protein at E14.5, with both mRNA and protein broadly expressed
220 across upper layers, lower layers, and the intermediate zone by E16.5. However, neurons
221 having migrated to their ultimate position in upper layers almost exclusively express Satb2
222 rather than Bcl11b protein, in contrast to regions like the intermediate zone where neurons
223 migrate towards the cortical plate.
224
225 Thus, in contrast to *Bcl11b* in the adjacent lower layers, *Satb2* mRNA and protein expression
226 are divergent in developmental time and space. This divergence includes broad, early *Satb2*
227 mRNA expression despite Satb2 protein ultimately restricted to upper layers later in
228 development. Furthermore, while the distribution and colocalization of mRNA for *Bcl11b* and
229 *Satb2* neuronal programs remains broad and overlapping at E16.5, corresponding protein
230 expression is more exclusive, with the intermediate zone a transitory region where
231 specification at both the mRNA and protein levels are still lacking distinction.
232
233 **Translation establishes the balance of neuronal fates after broad transcription**
234 Given the unexpected finding of *Satb2* mRNA in early-born neural stem cells, we next sought
235 to monitor transcriptional activation of the *Satb2* locus, and employed a fate mapping approach
236 with the *Satb2*$^{Cre/+}$ mouse line (Ambrozkiewicz et al., 2017). A Cre expression cassette is
237 located in place of exon 2 at the *Satb2* locus, which allows for timed *in utero* electroporation of
238 Cre-inducible reporters like *loxP-STOP-loxP-tdTomato* that clonally labels cells with tdTomato
239 that have a history of *Satb2* transcription (*Satb2*^{tdTom}) (**Figure 4A**). Co-electroporation with an
240 *eGFP* plasmid serves as a generic label for all transfected cells.
241
242 Remarkably, we detected *Satb2*^{tdTom} cells in the ventricular zone as early as E12.5 forming
243 clusters resembling clones or undergoing mitotic divisions (**Figure 4B**), and express neural
244 progenitor markers like Pax6 (apical progenitors) or Tbr2 (intermediate progenitors) (**Figure**
245 **4C**). *Satb2* transcription was observed for progenitors in the neocortex, but not in adjacent

brain regions (**Figure S4C**). Thus, early *Satb2* transcriptional priming occurs in early-born neocortex neural stem cells.

The balance of the Bcl11b vs. Satb2 lineages is essential for normal neocortex development and function. Satb2 directly suppresses the *Bcl11b* genomic enhancer, and loss of Satb2 engenders ectopic expression of *Bcl11b* in upper layer neurons, leading abnormal connectivity (Britanova et al., 2008). Therefore, we next investigated the expression of Bcl11b and Satb2 protein in cells that transcribe *Satb2* mRNA (**Figure 4D-E, Table S4**). Among cells transcribing *Satb2* mRNA, ~70% express Satb2 protein and ~30% express Bcl11b protein. Taken together, this observation indicates that despite unexpectedly broad and early transcription of the neuronal fate gene *Satb2*, translation of Satb2 protein restricts its expression to a late-born neuronal subtype, and crucially maintains the balance of alternative neuronal fates.

Translation downregulation decreases ribosome levels acutely at mid-neurogenesis E15.5

We next focused on genes that are translationally downregulated across neurogenesis after E12.5. Gene ontology analysis highlighted structural constituents of the ribosome, predominantly ribosomal proteins, as strongly downregulated by translation (**Figure 5A**). We calculated the developmental expression trajectory of all ribosomal proteins in the large and small subunits by RNA-seq, Ribo-seq, mass spec, and translation efficiency (**Figure 5B**). Results showed downregulation of nearly all ribosomal proteins at the Ribo-seq and MS level occurs acutely at E15.5, in advance of changes measured by RNA-seq, and reflecting translation downregulation until mid-neurogenesis. Decreasing ribosome levels by downregulation of ribosomal protein translation likely represents the coordinated regulation of this specific gene family, rather than a simple translation feedback loop, since numerous genes in other families undergo translation upregulation concurrently, such as chromatin binding proteins.

To visualize changing ribosome numbers sub-cellularly at high resolution, we performed immuno-electron microscopy analysis labeling ribosomal protein uS7 at E12.5 and E15.5 in the neocortex (**Figures 5C-D and S5, Table S4**). A striking difference in ribosome number was observed in differentiating neurons between early and late stages. Ribosomes are abundant in cortical plate neurons at E12.5, but scarce in both upper and lower layer neurons of the cortical

plate at E15.5. Notably, a progressive increase in ribosome number was observed as newly born neurons traverse away from the ventricular zone into the cortical plate at E12.5; while at E15.5, ribosome numbers decrease precipitously outside the ventricular zone, with few ribosomes measured in sub-ventricular zone progenitors. Thus, ribosome number is temporally encoded by translation at mid-gestation. As ribosome abundance is a powerful determinant of translation kinetics and selectivity (Mills and Green, 2017; Shah et al., 2013), global shifts in translation activity may occur at mid-neurogenesis.

Ribosome density at the start codon and within the CDS are developmentally dynamic

We next examined global translation activity during neocortex development by determining ribosome-mRNA interactions per-codon across all coding sequences. Ribosome position aligned to codons in the P-site demonstrated the characteristic 3-nucleotide periodicity in Ribo-seq metagene plots (**Figure 6A**). Ribosome occupancy surrounding the start codon increases sharply at E15.5, with progressive increases per stage until P0, while stop codon occupancy demonstrates the opposite trend and occurs independent of start codon changes. We applied RiboDiPA (Li et al., 2020), a linear modeling framework designed for positional analysis of Ribo-seq signal, to pinpoint the ~5-fold ribosome occupancy changes to the 4 codon bin surrounding the start and stop (**Figure 6B**).

Increased ribosome occupancy of the first four codons over time could represent a narrowing bottleneck in the transition from initiation to elongation, or signify increasingly robust initiation of target mRNAs. We correlated fold changes in start codon occupancy with translation efficiency and found an inverse relationship, suggesting that early elongation events progressively slow over time for a large cohort of proteins (**Figure 6C**). Translation of the N-terminus may become increasingly rate-limiting during synthesis Sbno2 and Pcdhgc4, in contrast to Tuba1c and Tuba1b representing more processive translation during development. Thus, as ribosome levels decline at E15.5 to P0, translation at the 5'-end of coding sequences occurs more slowly.

We next investigated distinct positions where variations in ribosome density take place (O'Connor et al., 2016) (**Figure 6D**; see **Methods**). A narrow region consistent with the ribosomal A-site accounts for most of the codon-specific variation in ribosome occupancy. Variation in A-site occupancy was most pronounced at E12.5-E14, with an acute decrease at

312 E15.5-E17, and low variation by P0. Analysis of ribosome dwell time per codon – a measure of
313 the codon-specific speed of translation (Gobet et al., 2020) – demonstrated early
314 developmental "fast" or "slow" kinetics in the bimodal distribution of codon dwell times in the A-
315 site (**Figures 6E and S6A-B; Table S5**). At E15.5, codon dwell times begin to equalize,
316 progressively reaching a unimodal distribution by P0. Furthermore, ribosome density
317 occupying A-site codons negatively correlates with P-site density in the embryonic period, but
318 no correlation was measured after birth at P0 (**Figure 6F**). Thus, the A-site codon in particular
319 influences ribosome dwell time, which is a barrier most pronounced early in neurogenesis
320 when ribosome levels are highest, and less pronounced after mid-neurogenesis when
321 ribosome levels decline.
322
323 Varying ribosome dwell time on a codon might be attributable to the availability of a given
324 tRNA. Dwell time is strongly correlated with tRNA abundance in yeast (Fang et al., 2018; Riba
325 et al., 2019; Weinberg et al., 2016), but is less correlated in some mammalian systems (Gobet
326 et al., 2020; Ingolia et al., 2011). We measured levels of 151 tRNA isodecoders by quantitative
327 PCR (qPCR) array at each stage (**Figure S7, Table S5**) to determine if tRNA abundance is
328 responsible for driving ribosome dwell time differences in the developing neocortex. Usage-
329 corrected tRNA abundance (availability) (Gobet et al., 2020) and codon optimality –
330 the non-uniform decoding rate between synonymous codons (dos Reis et al., 2004) – failed to
331 show any correlation with ribosome dwell time at the A-site (**Figures S6C-D**).
332
333 However, we found that the amino acid coded for is a strong determinant of ribosome density
334 occupying A-site codons, with synonymous codons showing similar occupancy (**Figure 6G,**
335 **Table S5**). Codons for acidic amino acids are among those with the highest occupancy,
336 suggesting they represent a kinetic barrier in early development translation (Chadani et al.,
337 2017; Riba et al., 2019). E12.5-E14 accounts for the extremes of A-site differences between
338 amino acids and among synonymous codons, with a progressive, chronologic trend towards
339 equalized occupancy by P0. Notably, some amino acids like leucine and isoleucine are coded
340 for by both "fast" and "slow" synonymous codons, particularly apparent early in development,
341 such as the fast TTA-Leu and slow CTG-Leu. Neither codon optimality (**Figure S6D**) nor
342 codon rarity would account for such dwell time differences, as TTA-Leu is a relatively rare
343 codon (Quax et al., 2015) with a short dwell time, while CTG-Leu is more common with a long
344 dwell time.

Taken together, “fast” and “slow” amino acids in the ribosome A-site characterize the early neurogenesis period when ribosome levels are transiently abundant, while ribosome accumulation at the start codon occurs late in neurogenesis when ribosome levels decline. These data strongly indicate that the fundamental kinetics of translation shift sharply at mid-neurogenesis, coinciding with major transitions in neuronal fate.

The ribosomal protein translation inhibitor eIF4EBP1 impacts neuronal fate and migration

To gain mechanistic insights into how timed translation regulation influences neurogenesis, we first analyzed mRNAs for sequence motifs in their untranslated regions (UTRs), which are powerful regulators of neocortical translation by RNA-binding proteins (DeBoer et al., 2013; Lennox et al., 2018; Zahr et al., 2019). Distinct motifs are enriched in the 5’- and 3’-UTRs of mRNAs with increasing or decreasing translation efficiency (**Figure 7A**). Translation downregulation motifs were only detected in 5’-UTRs and are enriched for terminal oligopyrimidine (5’-TOP) sequences. In translation upregulated mRNAs by contrast, 5’ GC-rich sequences and/or 3’ Pumilio binding motifs are prevalent. 5’-TOP sequences are a particular feature of ribosomal proteins coding mRNAs, and lead to their concerted translation downregulation when directly bound by their major upstream regulator eIF4EBP1 (**Figure 7B**) (Jin et al., 2020; Thoreen et al., 2012). Since we found that ribosome levels are controlled by a timed decrease in ribosomal protein translation, we next focused on how eIF4EBP1 expression coincides with translation regulation during neocortex development.

Western blot analysis demonstrated eIF4EBP1 levels change during neocortex development, with high expression at early stages until E15.5, followed by a sharp decrease at E17, and moderate recovery at P0 (**Figure 7C**). eIF4EBP1 levels coincide with the translation downregulation of ribosomal protein expression measured until E15.5, after which translation inhibition is transiently released at E17 (**Figures 5B and 7C, bottom**). These data strongly suggest eIF4EBP1 regulates the temporal shift in ribosome levels, which may impact timed translation of neuronal fate proteins like Satb2.

We next assessed the developmental expression of eIF4EBP1 *in situ* by immunohistochemistry analysis in the neocortex (**Figure 7D**). Robust eIF4EBP1 expression

378 was observed in neural stem cells at E12.5-E15.5 in the ventricular zone, with lower
379 expression in cortical plate neurons. At E17, eIF4EBP1 levels decrease throughout both stem
380 cell and neuronal zones, with some recovery at P0. These data suggest eIF4EBP1 may play a
381 role in the early-mid neurogenic period.
382
383 To measure the impact of eIF4EBP1 on neuronal fate during neocortex neurogenesis, we
384 performed shRNA knockdown by *in utero* electroporation in ventricular zone progenitors at
385 E13.5 when eIF4EBP1 levels are high, followed by immunohistochemistry assessment of
386 Satb2 protein expression at E15.5 when translation regulation dynamics peak (**Figure 7E**).
387 eIF4EBP1 knockdown in early progenitors leads to a decrease in the fraction of Satb2 protein
388 expressing neurons at E15.5 compared to scrambled control, and arrests neuronal entry into
389 the cortical plate (**Figure 7F, Table S4**). These data indicate that eIF4EBP1 impacts neuronal
390 fate and migration during a large-scale transient shift in translation activity at mid-gestation.
391

392 **DISCUSSION**

393 Our study traces how functional gene expression is catalyzed in a complex developmental
394 system, capturing the reactants, synthesis, and products of mRNA translation across the time
395 course of neocortex neurogenesis. We find widespread deviations in the trajectory of mRNA
396 and protein expression, along with changes in translation for ~18% of the transcriptome that
397 transiently peak at mid-neurogenesis. We interrogate the protein families most enriched
398 among translation up and downregulated genes. Translation upregulation particularly impacts
399 chromatin binding proteins like Satb2, which are master drivers of distinct neuronal lineages
400 (**Figure 7G**). Translation downregulation targets the translation machinery itself, with an acute
401 decline in ribosome number at mid-neurogenesis. The transition from relative ribosome
402 abundance to depletion is accompanied by a chronological shift in translation processivity at
403 the start codon and A-site amino acid during peptide elongation (**Figure 7H**). eIF4EBP1, the
404 major upstream suppressor of ribosomal protein translation efficiency, is dynamically
405 expressed during neurogenesis in tandem with ribosome abundance, and impacts Satb2
406 neuronal fate specification. Taken together, our data indicate that translation kinetics shift
407 during a critical window at mid-gestation to specify neuronal fate.
408
409 Neural stem cells harbor a pool of mRNAs inclusive of diverse neuronal fates, recently
410 described as “generic” (Telley et al., 2019), which has led the field to ask recently whether

411 neuronal subtype specification in the brain is a stochastic rather than deterministic process
412 (Llorca et al., 2019). Do “progenitors play dice” (Klingler and Jabaudon, 2020) while deciding
413 their neuronal fate? We propose that a broad transcriptome is filtered at the protein level for
414 tightly timed, rapidly scalable, and spatially targeted gene expression to assemble highly
415 evolved neuronal circuits. Per gene per hour, translation is faster and more scalable than
416 transcription by orders of magnitude (Schwanhäusser et al., 2009), and neuronal specification
417 transitions occur in very narrow developmental windows. The availability of a diverse mRNA
418 repertoire including both lower and upper layer neuronal fates like *Bcl11b* and *Satb2*,
419 respectively, which can be rapidly and selectively amplified by translation upregulation, is
420 essential to specify Bcl11b or Satb2 protein exclusive neurons, in addition to Bcl11b-Satb2
421 double-positive neurons (Nowakowski et al., 2017). Our translatome data provide a unique
422 window into how the proteome emerges from the transcriptome in neurodevelopment
423 (https://shiny.mdc-berlin.de/cortexomics/).
424
425 The timed decrease in ribosome number per cell in the cortical plate represents a coordinated
426 translation downregulation of ribosomal protein synthesis. The overwhelming influence that
427 changes in ribosome number can have on global protein synthesis kinetics and mRNA-specific
428 translation is strongly supported by theoretical and experimental data, and leads to
429 “ribosomopathies” in disease states (Mills and Green, 2017; Shah et al., 2013). With the role of
430 eIF4EBP1 early in neurogenesis, our study joins an evolving body of work on RNA-binding
431 proteins and ribosome cofactors that modulate protein synthesis in the developing brain
432 (DeBoer et al., 2013; Kraushar et al., 2014, 2021; Lennox et al., 2018; Popovitchenko et al.,
433 2020; Zahr et al., 2018, 2019). eIF4EBP1 is a master regulator of ribosome levels by
434 suppressing ribosomal protein synthesis (Jin et al., 2020; Thoreen et al., 2012), which we find
435 also impacts the fate and migration of a neuronal lineage prenatally. A timed mechanism to
436 finely tune ribosome levels may impose essential control on how and when proteins are
437 synthesized during neuronal fate decisions.
438
439 We measure a timed, progressive developmental shift in ribosome density surrounding start
440 and stop codons. Previous studies of the “5’ ramp” present in Ribo-seq experiments have
441 proposed that it represents ‘slow’ synonymous codon choice near the coding sequence start –
442 an adaptation to prevent ribosome collision further into the open reading frame (Pechmann
443 and Frydman, 2013). Our data argue against this as the sole mechanism of 5’ ramping, since

444 numerous genes show an increase in start density despite the generally decreasing effect of
445 codon choice. The increasing relative density at the 5' of many mRNA coding sequences
446 resembles what might be expected during a shift from ribosome abundant elongation-limited to
447 ribosome scarce initiation-limited translation (Heyer and Moore, 2016), when kinetic barriers to
448 start codon initiation and elongation of early N-terminal peptides (Verma et al., 2019) become
449 comparatively prominent. Of note, we do not observe increasing start codon density only for
450 high translation efficiency genes, or correlation with neurite-localized translation (**Figure S8**).
451 We therefore favor the hypothesis that ribosome occupancy at beginning of open reading
452 frames becomes progressively rate-limiting for codon-independent reasons, such as scarcity of
453 translation cofactors and ribosomal subunits later in development.
454
455 We also find that the A-site amino acid strongly influences translation speed during early
456 neurogenesis in particular, suggesting that factors like the electrostatics of peptidyl chain
457 elongation (Chadani et al., 2017; Riba et al., 2019), amino acid availability, and/or tRNA
458 aminoacylation might play a more important role in early brain development. To our knowledge,
459 our study is the first to demonstrate differences in the fundamental nature of codon-specific
460 ribosome density over developmental time. Our study agrees with previous work that suggest
461 tRNA levels are not a limiting factor for translation elongation in mammals (Gingold et al.,
462 2014; Gobet et al., 2020; Ingolia et al., 2011), as they are in exponentially dividing yeast (Fang
463 et al., 2018; Riba et al., 2019; Weinberg et al., 2016). Notably, however, these findings do not
464 rule out individual cases where a tRNA may influence ribosome stalling, as reported for one
465 nervous system-specific tRNA postnatally (Ishimura et al., 2014). We measure the total tRNA
466 pool by qPCR array with a protocol that does not address tRNA charging, which is a limitation
467 of our study and an interesting future direction.
468
469 The main limitation of our study is that parallel time course measurements of the transcriptome,
470 tRNA pool, translatome, and proteome occur in brain tissue of mixed cell types rather than
471 single cells. In addition to scRNA-seq, tremendous advances in analysis of the single-cell
472 translatome by Ribo-seq (Vaninsberghe et al., 2021) were just published. While development
473 of single-cell proteomics is still underway (Brunner et al., 2020; Slavov, 2020), the input
474 requirements for tRNA measurement remain a major obstacle. At the expense of cellular
475 resolution, we opted to perform a comprehensive analysis that enables modeling of mRNA
476 translation in developing brain tissue. Notably, while our study is well designed to measure

477 changes in protein synthesis, we do not measure protein degradation directly. The
478 unexpectedly large number of “MSdev” proteins identified in our model indicates that post-
479 translational mechanisms like degradation (Ambrozkiewicz and Kawabe, 2015; Ambrozkiewicz
480 et al., 2018; Chiang et al., 2021) can have a major impact by decoupling protein and Ribo-seq
481 trajectories, highlighting the complexity of gene regulation in the neocortex. Despite these
482 limitations, our approach detected two important phenomena validated at the cell type-specific
483 level – mRNA-protein uncoupling of Satb2 by translation upregulation, and coordinated
484 translation downregulation of ribosome number. Bulk tissue measurements can be very
485 informative in tandem with single cell data deconvolution in the brain (Harris et al., 2021; Jew
486 et al., 2020; Wang et al., 2019), and we anticipate our data will be leveraged as more single
487 cell technologies emerge.
488
489 Taken together, our data suggests a model of developmental gene expression where the
490 fundamental levels and kinetics of translation shift during a key window of neurogenesis in the
491 brain – creating a major inflection point of translation at mid-gestation (**Figures 7G-H**). These
492 developmental windows correspond to timed changes in neuronal specification from neural
493 stem cells, where broad transcription of neuronal subtype-specific programs is ultimately
494 refined by translational control, more precisely demarcating the boundaries of neuronal circuits
495 in the brain.
496

497 **ACKNOWLEDGEMENTS**

498 We thank Nadja Klein for advice regarding modeling and statistics, and Heike Heilmann for
499 support with immuno-electron microscopy. M.L.K. would like to thank Martin Vingron for
500 support. M.L.K. was funded by an EMBO Long-Term Postdoctoral Fellowship (190-2016),
501 Alexander von Humboldt Foundation Postdoctoral Fellowship, and International Guest
502 Fellowship from the Max Planck Institute for Molecular Genetics. D.H. was supported by a
503 grant from the Klaus Tschira Boost Fund. *In utero* electroporation experiments were funded by
504 a Russian Science Foundation Basic Research grant (19-34-51009) to V.T.
505

506 **AUTHOR CONTRIBUTIONS**

507 M.L.K. designed and initiated the study, with D.H. and M.C.A. making essential contributions.
508 U.O. and V.T. supervised the study, with contributions from C.M.T.S., M.L., M.S., and T.M.
509 Computational experiments were performed by D.H., and laboratory experiments by M.C.A.,

M.L.K., A.R., E.B., and R.D. Ribo-seq and RNA-seq sample preparation and sequencing were performed by U.Z. and M.L.K., and mass spectrometry sample preparation and measurement by K.I. and M.L.K. Immuno-electron microscopy samples were prepared by A.M.-W. and imaged by B.F. and M.L.K. Data were interpreted by D.H., M.C.A., and M.L.K. Manuscript figures and text were composed by D.H., M.C.A., and M.L.K., with valuable editing and input from all authors.

DECLARATION OF INTERESTS

The authors declare no competing interests.

REFERENCES

Ahmed, N., Sormanni, P., Ciryam, P., Vendruscolo, M., Dobson, C.M., and O'Brien, E.P. (2019). Identifying A- and P-site locations on ribosome-protected mRNA fragments using Integer Programming. Sci. Rep. *9*, 6256.

Alcamo, E. a., Chirivella, L., Dautzenberg, M., Dobreva, G., Fariñas, I., Grosschedl, R., and McConnell, S.K. (2008). Satb2 Regulates Callosal Projection Neuron Identity in the Developing Cerebral Cortex. Neuron *57*, 364–377.

Ambrozkiewicz, M.C., and Kawabe, H. (2015). HECT-type E3 ubiquitin ligases in nerve cell development and synapse physiology. FEBS Lett. *589*, 1635–1643.

Ambrozkiewicz, M.C., Bessa, P., Salazar-Lázaro, A., Salina, V., and Tarabykin, V. (2017). Satb2 Cre/+ mouse as a tool to investigate cell fate determination in the developing neocortex. J. Neurosci. Methods *291*, 113–121.

Ambrozkiewicz, M.C., Schwark, M., Kishimoto-Suga, M., Borisova, E., Hori, K., Salazar-Lázaro, A., Rusanova, A., Altas, B., Piepkorn, L., Bessa, P., et al. (2018). Polarity Acquisition in Cortical Neurons Is Driven by Synergistic Action of Sox9-Regulated Wwp1 and Wwp2 E3 Ubiquitin Ligases and Intronic miR-140. Neuron *100*, 1097-1115.e15.

Ambrozkiewicz, M.C., Borisova, E., Schwark, M., Ripamonti, S., Schaub, T., Smorodchenko, A., Weber, A.I., Rhee, H.J., Altas, B., Yilmaz, R., et al. (2020). The murine ortholog of Kaufman oculocerebrofacial syndrome protein Ube3b regulates synapse number by ubiquitinating Ppp3cc. Mol. Psychiatry *26*, 1980–1995.

Arlotta, P., Molyneaux, B.J., Chen, J., Inoue, J., Kominami, R., and Macklis, J.D. (2005). Neuronal subtype-specific genes that control corticospinal motor neuron development in vivo. Neuron *45*, 207–221.

Becker, K., Bluhm, A., Casas-Vila, N., Dinges, N., Dejung, M., Sayols, S., Kreutz, C., Roignant, J.Y., Butter, F., and Legewie, S. (2018). Quantifying post-transcriptional regulation in the development of Drosophila melanogaster. Nat. Commun. *9*, 4970.

Britanova, O., de Juan Romero, C., Cheung, A., Kwan, K.Y., Schwark, M., Gyorgy, A., Vogel, T., Akopov, S., Mitkovski, M., Agoston, D., et al. (2008). Satb2 Is a Postmitotic Determinant for

548 Upper-Layer Neuron Specification in the Neocortex. Neuron *57*, 378–392.

549 Brunner, A.-D., Thielert, M., Vasilopoulou, C., Ammar, C., Coscia, F., Mund, A., Horning, O.B.,
550 Bache, N., Apalategui, A., Lubeck, M., et al. (2020). Ultra-high sensitivity mass spectrometry
551 quantifies single-cell proteome changes upon perturbation. BioRxiv.

552 Buccitelli, C., and Selbach, M. (2020). mRNAs, proteins and the emerging principles of gene
553 expression control. Nat. Rev. Genet. *21*, 630–644.

554 Cadwell, C.R., Bhaduri, A., Mostajo-Radji, M.A., Keefe, M.G., and Nowakowski, T.J. (2019).
555 Development and Arealization of the Cerebral Cortex. Neuron *103*, 980–1004.

556 Calviello, L., Sydow, D., Harnett, D., and Ohler, U. (2019). Ribo-seQC: comprehensive
557 analysis of cytoplasmic and organellar ribosome profiling data. BioRxiv.

558 Chadani, Y., Niwa, T., Izumi, T., Sugata, N., Nagao, A., Suzuki, T., Chiba, S., Ito, K., and
559 Taguchi, H. (2017). Intrinsic Ribosome Destabilization Underlies Translation and Provides an
560 Organism with a Strategy of Environmental Sensing. Mol. Cell *68*, 528–539.

561 Chiang, S.Y., Wu, H.C., Lin, S.Y., Chen, H.Y., Wang, C.F., Yeh, N.H., Shih, J.H., Huang, Y.S.,
562 Kuo, H.C., Chou, S.J., et al. (2021). Usp11 controls cortical neurogenesis and neuronal
563 migration through Sox11 stabilization. Sci. Adv. *7*, eabc6093.

564 Cox, J., and Mann, M. (2008). MaxQuant enables high peptide identification rates,
565 individualized p.p.b.-range mass accuracies and proteome-wide protein quantification. Nat.
566 Biotechnol. *26*, 1367–1372.

567 Cox, J., Neuhauser, N., Michalski, A., Scheltema, R.A., Olsen, J. V., and Mann, M. (2011).
568 Andromeda: A peptide search engine integrated into the MaxQuant environment. J. Proteome
569 Res. *10*, 1794–1805.

570 Cox, J., Hein, M.Y., Luber, C.A., Paron, I., Nagaraj, N., and Mann, M. (2014). Accurate
571 Proteome-wide Label-free Quantification by Delayed Normalization and Maximal Peptide Ratio
572 Extraction, Termed MaxLFQ. Mol. Cell. Proteomics *13*, 2513–2526.

573 Cui, H., Hu, H., Zeng, J., and Chen, T. (2019). DeepShape: Estimating isoform-level ribosome
574 abundance and distribution with Ribo-seq data. BMC Bioinformatics.

575 DeBoer, E.M., Kraushar, M.L., Hart, R.P., and Rasin, M.R. (2013). Post-transcriptional
576 regulatory elements and spatiotemporal specification of neocortical stem cells and projection
577 neurons. Neuroscience *248*, 499–528.

578 Dobin, A., Davis, C.A., Schlesinger, F., Drenkow, J., Zaleski, C., Jha, S., Batut, P., Chaisson,
579 M., and Gingeras, T.R. (2013). STAR: ultrafast universal RNA-seq aligner. Bioinformatics *29*,
580 15–21.

581 Dunn, J.G., Foo, C.K., Belletier, N.G., Gavis, E.R., and Weissman, J.S. (2013). Ribosome
582 profiling reveals pervasive and regulated stop codon readthrough in Drosophila melanogaster.
583 Elife *2*, 1–32.

584 Fang, H., Huang, Y.F., Radhakrishnan, A., Siepel, A., Lyon, G.J., and Schatz, M.C. (2018).
585 Scikit-ribo Enables Accurate Estimation and Robust Modeling of Translation Dynamics at
586 Codon Resolution. Cell Syst. *6*, 180-191.e4.

587 Frederikson, K., and McKay, R.D.G. (1988). Proliferation and differentiation of rat
588 neuroepithelial precursor cells in vivo. J. Neurosci. *8*, 1144–1151.

589 Gingold, H., Tehler, D., Christoffersen, N.R., Nielsen, M.M., Asmar, F., Kooistra, S.M.,
590 Christophersen, N.S., Christensen, L.L., Borre, M., Sørensen, K.D., et al. (2014). A dual
591 program for translation regulation in cellular proliferation and differentiation. Cell *158*, 1281–
592 1292.

593 Gobet, C., Weger, B.D., Marquis, J., Martin, E., Neelagandan, N., Gachon, F., and Naef, F.
594 (2020). Robust landscapes of ribosome dwell times and aminoacyl-tRNAs in response to
595 nutrient stress in liver. Proc. Natl. Acad. Sci. U. S. A. *117*, 9630–9641.

596 Greig, L.C., Woodworth, M.B., Galazo, M.J., Padmanabhan, H., and Macklis, J.D. (2013).
597 Molecular logic of neocortical projection neuron specification, development and diversity. Nat.
598 Rev. Neurosci. *14*, 755–769.

599 Hahne, F., and Ivanek, R. (2016). Visualizing genomic data using Gviz and bioconductor. In
600 Methods in Molecular Biology, (Humana Press Inc.), pp. 335–351.

601 Harris, B.D., Crow, M., Fischer, S., and Gillis, J. (2021). Single-cell co-expression analysis
602 reveals that transcriptional modules are shared across cell types in the brain. Cell Syst. *12*,
603 748-756.e3.

604 Heyer, E.E., and Moore, M.J. (2016). Redefining the Translational Status of 80S Monosomes.
605 Cell *164*, 757–769.

606 Hoye, M.L., and Silver, D.L. (2021). Decoding mixed messages in the developing cortex:
607 translational regulation of neural progenitor fate. Curr. Opin. Neurobiol. *66*, 93–102.

608 Ingolia, N.T. (2016). Ribosome Footprint Profiling of Translation throughout the Genome. Cell
609 *165*, 22–33.

610 Ingolia, N.T., Ghaemmaghami, S., Newman, J.R.S., and Weissman, J.S. (2009). Genome-
611 wide analysis in vivo of translation with nucleotide resolution using ribosome profiling. Science.
612 *324*, 218–223.

613 Ingolia, N.T., Lareau, L.F., and Weissman, J.S. (2011). Ribosome profiling of mouse
614 embryonic stem cells reveals the complexity and dynamics of mammalian proteomes. Cell *147*,
615 789–802.

616 Ishimura, R., Nagy, G., Dotu, I., Zhou, H., Yang, X.-L.L., Schimmel, P., Senju, S., Nishimura,
617 Y., Chuang, J.H., and Ackerman, S.L. (2014). Ribosome stalling induced by mutation of a
618 CNS-specific tRNA causes neurodegeneration. Science. *345*, 455–459.

619 Jew, B., Alvarez, M., Rahmani, E., Miao, Z., Ko, A., Garske, K.M., Sul, J.H., Pietiläinen, K.H.,
620 Pajukanta, P., and Halperin, E. (2020). Accurate estimation of cell composition in bulk
621 expression through robust integration of single-cell information. Nat. Commun. *11*, 1971.

622 Jin, H., Xu, W., Rahman, R., Na, D., Fieldsend, A., Song, W., Liu, S., Li, C., and Rosbash, M.
623 (2020). TRIBE editing reveals specific mRNA targets of eIF4E-BP in Drosophila and in
624 mammals. Sci. Adv. *6*, eabb8771.

625 Josephson, R., Müller, T., Pickel, J., Okabe, S., Reynolds, K., Turner, P.A., Zimmer, A., and

McKay, R.D.G. (1998). POU transcription factors control expression of CNS stem cell-specific genes. Development *125*, 3087–3100.

Jovanovic, M., Rooney, M., Mertins, P., Przybylski, D., Satija, R., Rodriguez, E.H., Fields, A.P., Schwartz, S., Raychowdhury, R., Mumbach, M., et al. (2015). Dynamic profiling of the protein life cycle in response to pathogens. Science. *347*, 1259038.

Kalish, B.T., Kim, E., Finander, B., Duffy, E.E., Kim, H., Gilman, C.K., Yim, Y.S., Tong, L., Kaufman, R.J., Griffith, E.C., et al. (2021). Maternal immune activation in mice disrupts proteostasis in the fetal brain. Nat. Neurosci. *24*, 204–213.

Kim, D., Pertea, G., Trapnell, C., Pimentel, H., Kelley, R., and Salzberg, S.L. (2013). TopHat2: accurate alignment of transcriptomes in the presence of insertions, deletions and gene fusions Daehwan. Genome Biol. *14*, R36.

Klingler, E., and Jabaudon, D. (2020). Do progenitors play dice? Elife *9*, e54042.

Kraushar, M.L., Thompson, K., Wijeratne, H.R.S., Viljetic, B., Sakers, K., Marson, J.W., Kontoyiannis, D.L., Buyske, S., Hart, R.P., and Rasin, M.-R. (2014). Temporally defined neocortical translation and polysome assembly are determined by the RNA-binding protein Hu antigen R. Proc. Natl. Acad. Sci. USA *111*, E3815-24.

Kraushar, M.L., Viljetic, B., Wijeratne, H.R.S., Thompson, K., Jiao, X., Pike, J.W., Medvedeva, V., Groszer, M., Kiledjian, M., Hart, R.P., et al. (2015). Thalamic WNT3 Secretion Spatiotemporally Regulates the Neocortical Ribosome Signature and mRNA Translation to Specify Neocortical Cell Subtypes. J. Neurosci. *35*, 10911–10926.

Kraushar, M.L., Popovitchenko, T., Volk, N.L., and Rasin, M.-R. (2016). The frontier of RNA metamorphosis and ribosome signature in neocortical development. Int. J. Dev. Neurosci. *55*, 131–139.

Kraushar, M.L., Krupp, F., Turko, P., Ambrozkiewicz, M.C., Sprink, T., Imami, K., Vieira-Vieira, C.H., Schaub, T., Harnett, D., Münster-Wandowski, A., et al. (2021). Protein synthesis in the developing neocortex at near-atomic resolution reveals Ebp1-mediated neuronal proteostasis at the 60S tunnel exit. Mol. Cell *81*, 1–19.

Langmead, B., and Salzberg, S.L. (2012). Fast gapped-read alignment with Bowtie 2. Nat. Methods *9*, 357–359.

Law, C.W., Chen, Y., Shi, W., and Smyth, G.K. (2014). Voom: Precision weights unlock linear model analysis tools for RNA-seq read counts. Genome Biol.

Lennox, A.L., Mao, H., and Silver, D.L. (2018). RNA on the brain: emerging layers of post-transcriptional regulation in cerebral cortex development. WIREs Dev. Biol. *7*, e290.

Li, J.J., Bickel, P.J., and Biggin, M.D. (2014). System wide analyses have underestimated protein abundances and the importance of transcription in mammals. PeerJ *2*, e270.

Li, K., Hope, C.M., Wang, X.A., and Wang, J.P. (2020). RiboDiPA: a novel tool for differential pattern analysis in Ribo-seq data. Nucleic Acids Res. *48*, 12016–12029.

Llorca, A., Ciceri, G., Beattie, R., Wong, F.K., Diana, G., Serafeimidou-Pouliou, E., Fernández-Otero, M., Streicher, C., Arnold, S.J., Meyer, M., et al. (2019). A stochastic framework of

neurogenesis underlies the assembly of neocortical cytoarchitecture. Elife *8*, e51381.

Martin, M. (2011). Cutadapt removes adapter sequences from high-throughput sequencing reads. EMBnet.Journal *17*, 10.

McLeay, R.C., and Bailey, T.L. (2010). Motif Enrichment Analysis: A unified framework and an evaluation on ChIP data. BMC Bioinformatics *11*, 165.

McShane, E., Sin, C., Zauber, H., Wells, J.N., Donnelly, N., Wang, X., Hou, J., Chen, W., Storchova, Z., Marsh, J.A., et al. (2016). Kinetic Analysis of Protein Stability Reveals Age-Dependent Degradation. Cell *167*, 803-815.e21.

Mills, E.W., and Green, R. (2017). Ribosomopathies: There's strength in numbers. Science. *358*, eaan2755.

Nowakowski, T.J., Bhaduri, A., Pollen, A.A., Alvarado, B., Mostajo-Radji, M.A., Di Lullo, E., Haeussler, M., Sandoval-Espinosa, C., Liu, S.J., Velmeshev, D., et al. (2017). Spatiotemporal gene expression trajectories reveal developmental hierarchies of the human cortex. Science. *358*, 1318–1323.

O'Connor, P.B.F., Andreev, D.E., and Baranov, P. V. (2016). Comparative survey of the relative impact of mRNA features on local ribosome profiling read density. Nat. Commun. *7*, 12915.

Pechmann, S., and Frydman, J. (2013). Evolutionary conservation of codon optimality reveals hidden signatures of cotranslational folding. Nat. Struct. Mol. Biol.

Popovitchenko, T., Park, Y., Page, N.F., Luo, X., Krsnik, Z., Liu, Y., Salamon, I., Stephenson, J.D., Kraushar, M.L., Volk, N.L., et al. (2020). Translational derepression of Elavl4 isoforms at their alternative 5′ UTRs determines neuronal development. Nat. Commun. *11*, 1674.

Quax, T.E.F., Claassens, N.J., Söll, D., and van der Oost, J. (2015). Codon Bias as a Means to Fine-Tune Gene Expression. Mol. Cell *59*, 149–161.

dos Reis, M., Savva, R., and Wernisch, L. (2004). Solving the riddle of codon usage preferences: A test for translational selection. Nucleic Acids Res. *32*, 5036–5044.

Riba, A., Di Nanni, N., Mittal, N., Arhné, E., Schmidt, A., and Zavolan, M. (2019). Protein synthesis rates and ribosome occupancies reveal determinants of translation elongation rates. Proc. Natl. Acad. Sci. *116*, 15023–15032.

Schindelin, J., Arganda-Carreras, I., Frise, E., Kaynig, V., Longair, M., Pietzsch, T., Preibisch, S., Rueden, C., Saalfeld, S., Schmid, B., et al. (2012). Fiji: An open-source platform for biological-image analysis. Nat. Methods *9*, 676–682.

Schwanhäusser, B., Gossen, M., Dittmar, G., and Selbach, M. (2009). Global analysis of cellular protein translation by pulsed SILAC. Proteomics *9*, 205–209.

Schwanhäusser, B., Busse, D., Li, N., Dittmar, G., Schuchhardt, J., Wolf, J., Chen, W., and Selbach, M. (2011). Global quantification of mammalian gene expression control. Nature *473*, 337–342.

Shah, P., Ding, Y., Niemczyk, M., Kudla, G., and Plotkin, J.B. (2013). Rate-limiting steps in

703 yeast protein translation. Cell *153*, 1589–1601.

704 Slavov, N. (2020). Unpicking the proteome in single cells. Science. 512–513.

705 Telley, L., and Jabaudon, D. (2018). A mixed model of neuronal diversity. Nature *555*, 452–
706 454.

707 Telley, L., Agirman, G., Prados, J., Amberg, N., Fièvre, S., Oberst, P., Bartolini, G., Vitali, I.,
708 Cadilhac, C., Hippenmeyer, S., et al. (2019). Temporal patterning of apical progenitors and
709 their daughter neurons in the developing neocortex. Science. *364*.

710 Thoreen, C.C., Chantranupong, L., Keys, H.R., Wang, T., Gray, N.S., and Sabatini, D.M.
711 (2012). A unifying model for mTORC1-mediated regulation of mRNA translation. Nature *485*,
712 109–113.

713 Tyanova, S., Temu, T., Sinitcyn, P., Carlson, A., Hein, M.Y., Geiger, T., Mann, M., and Cox, J.
714 (2016). The Perseus computational platform for comprehensive analysis of (prote)omics data.
715 Nat. Methods *13*, 731–740.

716 Vaninsberghe, M., Berg, J., Andersson-rolf, A., Clevers, H., and Oudenaarden, A. (2021).
717 Single-cell Ribo-seq reveals cell cycle-dependent translational pausing. Nature *597*, 561–565.

718 Verma, M., Choi, J., Cottrell, K.A., Lavagnino, Z., Thomas, E.N., Pavlovic-Djuranovic, S.,
719 Szczesny, P., Piston, D.W., Zaher, H.S., Puglisi, J.D., et al. (2019). A short translational ramp
720 determines the efficiency of protein synthesis. Nat. Commun. *10*, 5774.

721 Wang, X., Park, J., Susztak, K., Zhang, N.R., and Li, M. (2019). Bulk tissue cell type
722 deconvolution with multi-subject single-cell expression reference. Nat. Commun. *10*.

723 Weinberg, D.E., Shah, P., Eichhorn, S.W., Hussmann, J.A., Plotkin, J.B., and Bartel, D.P.
724 (2016). Improved Ribosome-Footprint and mRNA Measurements Provide Insights into
725 Dynamics and Regulation of Yeast Translation. Cell Rep. *14*, 1787–1799.

726 Xiao, Z., Zou, Q., Liu, Y., and Yang, X. (2016). Genome-wide assessment of differential
727 translations with ribosome profiling data. Nat. Commun. *7*, 1–11.

728 Zahr, S.K., Yang, G., Kazan, H., Borrett, M.J., Yuzwa, S.A., Voronova, A., Kaplan, D.R., and
729 Miller, F.D. (2018). A Translational Repression Complex in Developing Mammalian Neural
730 Stem Cells that Regulates Neuronal Specification. Neuron *97*, 520–537.

731 Zahr, S.K., Kaplan, D.R., and Miller, F.D. (2019). Translating neural stem cells to neurons in
732 the mammalian brain. Cell Death Differ. *26*, 2495–2512.

733 Zappulo, A., Van Den Bruck, D., Ciolli Mattioli, C., Franke, V., Imami, K., McShane, E.,
734 Moreno-Estelles, M., Calviello, L., Filipchyk, A., Peguero-Sanchez, E., et al. (2017). RNA
735 localization is a key determinant of neurite-enriched proteome. Nat. Commun. *8*, 583.

736

737 **STAR★METHODS**

738 **KEY RESOURCES TABLE**

REAGENT or RESOURCE	SOURCE	IDENTIFIER
Antibodies		
Goat anti-GFP	Rockland	600-101-215M; RRID:AB_2612804
Rabbit anti-Pax6	Millipore	AB2237; RRID:AB_1587367
Rabbit anti-Tbr2 / Eomes	Abcam	ab23345; RRID:AB_778267
Rabbit anti-Satb2	(Ambrozkiewicz et al., 2017)	N/A
Rat anti-Bcl11b (Ctip2)	Abcam	25B6; RRID:AB_2064130
Rabbit anti-Cre	Synaptic Systems	257003; RRID:AB_2619968
Donkey anti-goat AlexaFluor-488	Jackson Immunoresearch	705-546-147; RRID:AB_2340430
Donkey anti-rabbit AlexaFluor-488	Jackson Immunoresearch	711-545-152; RRID:AB_2313584
Donkey anti-rabbit AlexaFluor-Cy3	Jackson Immunoresearch	711-167-003; RRID:AB_2340606
Donkey anti-rabbit AlexaFluor-Cy3	Jackson Immunoresearch	711-165-152; RRID:AB_2307443
Mouse anti-Rps5 (uS7)	Santa Cruz	sc-390935; RRID:AB_2713966
Rabbit anti-eIF4EBP1	Abcam	ab32024; RRID:AB_2097990
Gold-conjugated-anti-mouse IgG	Nanoprobes	2001; RRID:AB_2877644

739

FISH Probes		
RNAscope Probe-Mm-Satb2	ACD, Bio-techne	413261
RNAscope Probe-Mm-Bcl11b-C2	ACD, Bio-techne	413271-C2

740

Recombinant DNA		
pCAG-eGFP	(Ambrozkiewicz et al., 2017)	N/A
pCAG-flox-STOP-flox-tdTomato	(Ambrozkiewicz et al., 2017)	N/A
Scrambled shRNA control	Thermo Scientific (Ambrozkiewicz et al., 2017)	N/A
eIF4EBP1 shRNA	Sigma Mission	TRCN0000335381

741

Chemicals, Peptides, and Recombinant Proteins		
Acetonitrile	CHEMSOLUTE	2697
Agarose	Sigma-Aldrich	A9539
Ammonium bicarbonate (ABC)	Sigma-Aldrich	9830

Bovine serum albumin	Sigma-Aldrich	A3294
DAPI (Nuc Blue, Molecular Probes)	Invitrogen	R37606
Dithiothreitol (DTT)	Sigma-Aldrich/Roche	DTT-RO
DNAse-I	Roche	4716728001
Ethanol	J.T. Baker	8025
Fetal Bovine Serum	Gibco	10270106
Formic acid	Sigma-Aldrich	33015
HEPES	Sigma-Aldrich	391338
IGEPAL CA-630	Sigma-Aldrich	I8896
Iodoacetamide (IAA)	Sigma-Aldrich	I6125
KCl	Roth	6781.1
Lysyl endopeptidase (LysC)	Wako	12505061
Methanol	Merck Millipore	1.06009.2511
$MgCl_2$	Ambion	AM9530G
Normal goat serum	PAN-Biotech	P30-1002
Paraformaldehye (PFA)	Sigma-Aldrich	P6148
Phenylmethyl sulphonyl fluoride (PMSF)	Roth	6367
Protease Inhibitor cOmplete EDTA-free	Roche	5056489001
ReproSil-Pur C18-AQ 3-µm resin	Dr. Maisch GmbH	r13.aq
RNasin Plus RNAse inhibitor	Promega	N2615
RNAse-T1	Thermo Fisher	eno541
RNAse-A	Thermo Fisher	eno531
Sodium dodecyl sulfate (SDS)	Roth	2326.1
Spermidine•3HCl	Sigma-Aldrich	S2501
Spermine•4HCl	Sigma-Aldrich	S2876
Sucrose	Sigma-Aldrich	S0389
SUPERase-In RNAse inhibitor	ThermoFisher	AM2694
Tris-HCl	Roth	9090.3
Triton-X 100	Sigma-Aldrich	T8787
TRIzol-LS	Invitrogen	10296010
Trypsin	Promega	V511A
TurboDNase	Thermo Fisher	AM2238
Tween	Sigma-Aldrich	P9416
Urea	Sigma-Aldrich	51459
Vectashield Mounting Medium	Vector Laboratories	H-1000

742

Critical Commercial Assays		
NEBNext Ultra Directional RNA Library Prep Kit for Illumina	New England BioLabs	E7420L
NEXTflex Small RNA-seq Kit v3	Bio Scientific	NOVA-5132-06
RNA Clean & Concentrator-25 Kit	Zymo Research	R1017
RiboZero Kit	Illumina	20037135
TruSeq Stranded mRNA Kit	Illumina	20020594
Zymoclean Gel DNA Recovery Kit	Zymo Research	D4007/D4008
RNAscope Multiplex Fluorescent Reagent Kit v2	ACD, Bio-techne	323100

743

Deposited Data		
Neocortex Ribosome Profiling	this paper	NIH GEO: GSE169457
Neocortex RNA-seq	(Kraushar et al., 2021)	NIH GEO: GSE157425
Neocortex tRNA qPCR Array	this paper	NIH GEO: GSE169621
Neocortex Mass Spectrometry	(Kraushar et al., 2021)	ProteomeXchange: PXD014841

744

Experimental Models: Organisms/Strains		
CD1 WT mice	Charles River	RRID:IMSR_CRL:22
NMRI WT mice	Charles River and Janvier Labs	RRID:IMSR_TAC:nmri
Satb2$^{Cre/+}$ mouse line	(Britanova et al., 2008)	N/A

745

Software and Algorithms		
Bcl2fastq	https://support.illumina.com/downloads/bcl2fastq-conversion-software-v2-20.html	2.20.0
Bowtie2	(Langmead and Salzberg, 2012)	
Cutadapt	(Martin, 2011)	
FIJI	(Schindelin et al., 2012)	https://fiji.sc/
GraphPad Prism 7	GraphPad Software Inc.	https://www.graphpad.com/
Gviz	(Hahne and Ivanek, 2016)	
IBAQ	(Schwanhäusser et al., 2011)	
Illustrator	Adobe Creative Cloud	
LFQ	(Cox et al., 2014)	
Limma	(Law et al., 2014)	
MaxQuant	(Cox and Mann, 2008)	
Meme	McLeay & Bailey, 2010	
Perseus	(Tyanova et al., 2016)	

Photoshop	Adobe Creative Cloud	
proDA	https://github.com/const-ae/proDA	
R v4.0.0	https://www.r-project.org/	
RiboDiPA	(Li et al., 2020)	
Ribo-seqC v1.1	https://github.com/ohlerlab/Ribo-seqC	
snakemake	https://academic.oup.com/bioinformatics/article/28/19/2520/290322	
SPSS v.17	IBM Inc.	
STAR	(Dobin et al., 2013)	
topGO	https://bioconductor.org/packages/release/bioc/html/topGO.html	
TopHat2	(Kim et al., 2013)	
tximport	https://f1000research.com/articles/4-1521/v1	
Xtail	(Xiao et al., 2016)	

CONTACT FOR REAGENT AND RESOURCE SHARING

Lead Contact

Further information and requests for reagents may be directed to and will be fulfilled by the Lead Contact, matthew.kraushar@molgen.mpg.de (M.L.K.).

Materials Availability

This study did not generate new unique reagents.

Data and Code Availability

Code generated during this study, not otherwise referenced in the **Methods**, is supplied at https://github.com/ohlerlab/cortexomics. Further requests may be directed to and will be fulfilled by the Lead Contact, matthew.kraushar@molgen.mpg.de (M.L.K.). Data have been deposited in publicly available repositories as indicated in the **Methods**.

EXPERIMENTAL MODEL AND SUBJECT DETAILS

Mice

Mouse (*Mus musculus*) lines were maintained in the animal facilities of the Charité University Hospital and Lobachevsky State University. All experiments were performed in compliance with the guidelines for the welfare of experimental animals approved by the State Office for Health and Social Affairs, Council in Berlin, Landesamt für Gesundheit und Soziales (LaGeSo),

767 permissions T0267/15, G0079/11, G206/16, and G54/19, and by the Ethical Committee of the
768 Lobachevsky State University of Nizhny Novgorod. Mice were utilized in the embryonic (E12.5-
769 E17) and early post-natal (P0) period, inclusive of both male and female sexes in each litter
770 without distinction. Timed pregnant wild-type (WT) CD-1 mice utilized for Ribo-seq, RNA-seq,
771 tRNA qPCR array, mass spectrometry, and immuno-electron microscopy were obtained from
772 the Charles River Company (Protocol: T0267/15). Experiments with fluorescent *in situ*
773 hybridization and immunohistochemistry (**Figures 3, 7, and S4A-B**) were performed in NMRI
774 WT mice. For experiments with the tdTomato reporter (**Figures 4 and S4C**), *Satb2*$^{Cre/+}$ males
775 (Britanova et al., 2008) were mated to NMRI wild type females (Protocols: G0079/11, G54/19,
776 and G206/16). *Satb2*$^{Cre/+}$ mouse genotyping was performed as described (Britanova et al.,
777 2008).
778

779 **METHOD DETAILS**

780 **Neocortex sample preparation for bioinformatics analysis**

781 Dissection, cryogenic lysis, and determination of optical density units (ODU) were performed
782 as described (Kraushar et al., 2021).
783

784 **Ribo-seq and RNA-seq sample preparation and sequencing**

785 Each replicate for paired neocortex Ribo-seq and RNA-seq included 40 brains (80
786 hemispheres) at E12.5, 30 brains (60 hemispheres) at E14, 21 brains (42 hemispheres) at
787 E15.5, 20 brains (40 hemispheres) at E17, and 17 brains (34 hemispheres) at P0 – performed
788 in biological duplicate at each stage. Neocortex tissue was lysed on ice in 20 mM HEPES,
789 100 mM KCl, 7.5 mM $MgCl_2$, pH 7.4, supplemented with 20 mM Dithiothreitol (DTT), 0.04 mM
790 Spermine, 0.5 mM Spermidine, 1x Protease Inhibitor cOmplete EDTA-free (Roche,
791 05056489001), 0.3% v/v IGEPAL CA-630 detergent (Sigma, I8896) and clarified by
792 centrifugation at 16100 x*g* for 5 min at 4 °C with a benchtop centrifuge. Samples were then
793 measured for A260 ODU on a NanoDrop 1000 Spectrophotometer. Two thirds of the sample
794 were transferred to a new tube for Ribo-seq preparation, with the remaining one third for RNA-
795 seq was mixed with 100 U SUPERase-In RNAse inhibitor (ThermoFisher, AM2694) and frozen
796 at -80 °C for downstream RNA isolation.
797

798 For digestion of ribosome protected RNA fragments (RPFs), Ribo-seq samples were then
799 mixed with 60U RNAse-T1 plus 96 ng RNAse-A per ODU (as optimized, **Figure S1A-B**), and

800 incubated for 30 min at 25 °C, shaking at 400 rpm. To stop RNAse activity, 200 U of
801 SUPERase-In RNAse inhibitor was then added.
802
803 10-50 % 5 mL sucrose density gradients were prepared in Beckman Coulter Ultra-Clear Tubes
804 (344057). Base buffer consisted of 20 mM HEPES, 100 mM KCl, 10 mM $MgCl_2$, 20 mM
805 Dithiothreitol (DTT), 0.04 mM Spermine, 0.5 mM Spermidine, 1x Protease Inhibitor cOmplete
806 EDTA-free (Roche, 05056489001), 20 U/mL SUPERase-In RNAse inhibitor (ThermoFisher,
807 AM2694), pH 7.4, prepared with 10 & 50 % sucrose w/v. Overlaid 10 & 50 % sucrose-buffer
808 solutions were mixed to linearized gradients with a BioComp Gradient Master 107ip.
809
810 Digested lysates were overlaid on gradients pre-cooled to 4 °C. Gradients were centrifuged in
811 a SW55 rotor (Beckman Coulter) for 1 hr, 4 °C, 37000 rpm, and fractionated using a BioComp
812 Piston Gradient Fractionator and Pharmacia LKB SuperFrac, with real-time A260
813 measurement by an LKB 22238 Uvicord SII UV detector recorded using an ADC-16
814 PicoLogger and associated PicoLogger software. Fractions corresponding digested 80S
815 monosomes (**Figure S1C**) were pooled and stored at -80 °C.
816
817 RNA isolation with TRIzol LS was then performed for both RNA-seq and Ribo-seq samples, as
818 per the manufacturer's instructions. For Ribo-seq and RNA-seq samples, downstream library
819 preparation and sequencing were performed as described (Kraushar et al., 2021). RNA-seq
820 data were utilized in a recent study (Kraushar et al., 2021) corresponding to NIH GEO
821 entry GSE157425. Ribo-seq data in this study are deposited in the NIH GEO: GSE169457.
822
823 **Mass spectrometry sample preparation**
824 Total proteome analysis from neocortex lysates at E12.5, E14, E15.5, E17, and P0, including
825 complete lysis in RIPA buffer, and downstream processing for mass spectrometry analysis,
826 was performed in a recent study (Kraushar et al., 2021) corresponding to ProteomeXchange
827 entry PXD014841.
828
829 **tRNA qPCR array sample preparation and measurement**
830 tRNA qPCR array measurement of 151 tRNA isodecoders was performed by Arraystar
831 (Maryland, USA) for neocortex lysates at E12.5, E14, E15.5, E17, and P0 from the same total

832 RNA isolated for RNA-seq described above (**Table S5**). Data are deposited in the NIH GEO:
833 GSE169621.
834
835 **Ribo-seq and RNA-seq data processing**
836 Raw sequence data was converted to FASTQ format using bcl2fastq. Adapters (sequence
837 TGGAATTCTCGGGTGCCAAGG) were removed from Ribo-seq reads with cutadapt, as well
838 as sequences with a quality score less than 20 or a remaining sequence length less than 12,
839 and after removing duplicate read sequences, 4bp UMIs were trimmed from either end of each
840 sequence using a custom perl script. Ribo-seq reads were then aligned to an index of common
841 contaminants (including tRNA, rRNA, and snoRNA sequences) using bowtie2. The resulting
842 processed read files were then aligned to coding sequences (the pc_transcripts fasta file), and
843 separately, to the genome, from GENCODE release M12 (*Mus musculus*) using STAR, with
844 the following settings: STAR --outSAMmode NoQS --outSAMattributes NH NM --
845 seedSearchLmax 10 --outFilterMultimapScoreRange 0 --outFilterMultimapNmax 255 --
846 outFilterMismatchNmax 1 --outFilterIntronMotifs RemoveNoncanonical. RNA-seq and Ribo-
847 seq libraries achieved high coverage, with a median of 33M and 12M reads mapped to protein
848 coding transcripts, respectively. For quality control, downstream analysis focused on coding
849 sequences with 32 or more Ribo-seq footprints in at least one stage as per (Dunn et al., 2013),
850 which resulted in a set of 12,228 translated gencode transcripts (**Table S1**).
851
852 For **Figures 1C, 2A, 3B, and 5B**, linear fold change for RNA-seq and Ribo-seq were
853 calculated using limma (Law et al., 2014), TEs were calculated using xtail, and MS fold
854 changes were calculated using proDA (**Table S2**).
855
856 Since ribosomes with their A-site over a given position will produce a distribution of read
857 lengths mapping to nearby positions, A/P-site alignment represents a crucial step in the
858 processing of Ribo-seq datasets. Frequently, algorithms for A-site alignment rely either
859 explicitly (Calviello et al., 2019; Fang et al., 2018) or implicitly (Ahmed et al., 2019;) on the
860 presence of large peaks at the start and/or stop codons, the known location of which provides
861 a 'true positive' that can be used to choose P-site offsets for each read length. We found that
862 such methods gave inconsistent results in our data, with optimal P-sites being chosen at
863 biochemically implausible values (e.g., at 0 base pairs from the read 5'-end). This is likely due
864 to 1) the variable occupancy of the start/stop peak in our data (**Figure 6A-B**), and 2) the

presence of cut-site bias in our data due to the necessity of RNAse T1 & A digestion (**Figure S6A-B**). Calculating RUST scores and 'metacodon' (O'Connor et al., 2016) plots of RPF 5'-end occurrence showed that the most variation between different codons and time points (other than cut-site bias itself at RPF termini) was nonetheless limited to a narrow region a consistent distance from the codon, for each read length (**Figure 6D**). Plotting KL-Divergence between observed and expected RUST scores at different distances from the read 5' end and measuring the between-codon variance at each position revealed that it aligned with an offset of approximately 14-15 nt (consistent with the A-site position) for reads of length between 25 and 31, and so we chose these for further analysis of ribosome dwell time (**Table S5**). We also observed an adjacent region of lesser variability 3bp towards the RPF 5' end, consistent with a non-zero but significantly less influence of the P-site codon (**Figure 6D and Table S5**).

The program DeepShapePrime (Cui et al., 2019), modified to accept our chosen P-site offsets instead of hardcoded ones, was then used to derive isoform specific abundance measurements for each protein coding transcript.

In parallel to the above, iso-form level quantification of the RNA-seq was carried out using salmon, with an index built from coding M12 sequences, and the following settings: salmon quant -l SR --seqBias --validateMappings

A snakemake file automating the above workflow is available at https://github.com/ohlerlab/cortexomics.

We then converted DeepShape-prime's output to salmon format to combine both outputs, using the ORF length as effective length. The R package tximport was used to derive length-corrected gene-level counts and isoform level counts and TPMs for both datasets. The voom package was used for variance stabilization and linear modelling of this data to derive confidence intervals for transcriptional and translational change, both relative to E12.5, and stepwise between each stage. The xTail package (Xiao et al., 2016), which is specifically geared towards estimation of translational efficiency (TE; i.e. the ratio of Ribo-seq density to RNA-seq density) change in the presence of transcriptional change, was used to detect changing TE. Numbers for TE change quoted in the text refer to xtail's differential TE calls,

897 with stepwise fold changes shown in **Figure 1**, and TE changing genes being elsewhere
898 defined relative to E12.5 (**Table S2**).
899
900 For metagene plots (**Figure 6A**), a 'best transcript' (the transcript with the highest median
901 Ribo-seq coverage across all samples) was selected for each gene. These transcripts were
902 further limited to those with a length of 192 or greater. Each of these transcripts was also also
903 analysed using the RiboDiPA package, which looks for position-specific differences in Ribo-
904 seq occupancy between conditions. Since metacodon plots indicated that changes at the start
905 and stop codon were limited to a distinct region 3-4 codons from the start and stop, we divided
906 each coding sequence in to 15 bins, with 7 bins of 4 codons each centering on the start and
907 stop, and a final 'mid' bin of variable size encompassing the rest of the ORF (ORFs too short to
908 accommodate this were excluded). We then plotted bin-level log2 fold changes for each gene
909 with significant q-value of using the AUG/stop changing bins (**Figure 6B**).
910
911 Fold changes were binarized into 'significant' (absolute fold change greater or less than 1.25,
912 adjusted p-value < 0.05) and 'non-significant' for up and down regulated genes respectively,
913 for plotting, and GO term analysis – referred to as dTE and non-dTE in the case of TE fold-
914 change. For GO term analyses of TE change and positional Ribo-seq change, The R package
915 topGO was used.
916
917 A list of ribosomal proteins for the mouse large and small subunits were curated from Uniprot.
918
919 **tRNA abundance and codon dwell time analysis**
920 tRNA abundance was calculated from Arraystar Ct values by the negative delta Ct value for
921 each tRNA compared to the mean of 5S and 18S rRNA levels in each sample (**Figure S7,**
922 **Table S5**). Abundance per-codon was calculated by taking the mean of each replicate, and
923 summing values for all relevant iso-decoders. Availability (Gobet et al., 2020) was calculated
924 as the residual from a simple linear model regressing codon usage against abundance, where
925 codon usage was defined as the occurrence of that codon in the M12 coding transcriptome,
926 weighted by the relevant TPM of each transcript in that sample. We attempted weighting by
927 wobble base pairs as in (dos Reis et al., 2004) and found this did not impact the conclusions in
928 **Figure 6**.
929

930 We followed the approach of (O'Connor et al., 2016) and used RUST values as a robust
931 estimator of codon specific dwell times. A-site occupancy was defined as the RUST value for
932 that codon at the point of maximum variation (14 or 15 base pairs from the 5' end) with P-site
933 occupancy defined as the RUST value 3bp closer to the 5' from there (see **Table S5**)
934
935 Relationships between codon dwell time, tRNA abundance/availability, and amino acid identity,
936 were investigated using the R function lm. The dataset used consisted of 269 – (i.e. one per
937 quantified codon, per sample) with terms for the stage of the sample (S), the amino acid coded
938 for (AA), and the abundance (or availability) of the encoding tRNAs (AB).
939
940 The largest explanatory variable was AA, which also showed a significant interaction with S,
941 indicating that the amino acid coded for explained ~ 34% of the variance in dwell time between
942 codons. This term also showed a significant interaction with sample stage, indicating that the
943 amino-acid specific factors determining dwell time may vary over development (e.g., due to the
944 availability of amino acids changing). Within a sample or across all samples, there was no
945 association between tRNA abundance and dwell time, even after correcting for the effect of
946 amino acid coded-for. Some codons however show a significant interaction between
947 abundance and developmental stage, and because these codons were biased towards the
948 high or low end of the abundance dwell time spectrum, we plotted time-relative change vs
949 abundance, for the top and bottom quartiles of dwell time abundance. This revealed a
950 significant association between change in time-relative tRNA abundance and dwell time, with
951 fastest codons showing decreasing tRNA abundance as they slowed, and the slowest codons
952 also showing decreasing tRNA abundance.
953
954 **Mass Spectrometry data processing**
955 All raw data were analyzed and processed by MaxQuant (v1.6.0.1) (**Table S1**) (Cox and Mann,
956 2008). Default settings were kept except that 'match between runs' was turned on. Search
957 parameters included two missed cleavage sites, cysteine carbamidomethyl fixed modification
958 and variable modifications including methionine oxidation, protein N-terminal acetylation and
959 deamidation of glutamine and asparagine. The peptide mass tolerance was 6ppm and the
960 MS/MS tolerance was 20ppm. Minimal peptide length of 7 amino acids was required.
961 Database search was performed with Andromeda (Cox et al., 2011) against the
962 UniProt/SwissProt mouse database (downloaded 01/2019) with common serum contaminants

963 and enzyme sequences. The false discovery rate (FDR) was set to 1% at peptide spectrum
964 match (PSM) level and at protein level. Protein quantification across samples was performed
965 using the label-free quantification (LFQ) algorithm (Cox et al., 2014). A minimum peptide count
966 required for LFQ protein quantification was set to two. Only proteins quantified in at least two
967 out of the three biological replicates were considered for further analyses.
968
969 To improve the match between mass spec data and sequence data, the peptides from each
970 mass spec group were matched against M12 protein sequences. Instances in which a
971 UNIPROT gene identifier did not match any gene in GENCODE, but in which the associated
972 peptide sequences matched proteins for a single GENCODE gene, were updated to match
973 that Gencode gene. All further analyses were carried out using gene-level proteomic data.
974
975 The R package proDA was used to calculate dropout-aware abundance estimates for each
976 protein group, as well as fold changes and confidence intervals relative to E12.5. For each
977 gene, a 'best' matching protein group was defined as the one with the least missing, and
978 highest median, signal across all samples, and selected for further analysis.
979
980 **Analysis of variance**
981 Analysis of variance was carried out a manner similar to (Li et al., 2014). We fit a linear model
982 regressing measured protein levels, or protein fold changes, P, against measured Ribo-seq or
983 RNA-seq levels R. We then performed variance decomposition using the following equation:
984

985 $$\hat{\sigma}^2_{\mathrm{PDT}} = \hat{\sigma}^2_{all} - \left(\frac{\hat{b}_{all}}{\hat{b}_R}\right)^2 \hat{\sigma}^2_R - \hat{\sigma}^2_P.$$

986 Where $\hat{\sigma}^2_{\mathrm{all}}$ represents total variance in measured protein abundance, (i.e. in proDA-normalized
987 LFQ values) and is decomposed into stochastic error in protein measurement $\hat{\sigma}^2_{\mathrm{P}}$ (estimated
988 standard error of the protein abundance model fit using proDA), systematic variation in protein
989 levels independent of R $\hat{\sigma}^2_{\mathrm{PDT}}$, and error in R measurement, where $\hat{b}_{all}$ is the linear coefficient
990 relating Ribo-seq and RNA-seq measurements to protein abundance, $\hat{b}_R$ is the measurement
991 bias for R, and $\hat{\sigma}^2_R$ s the stochastic measurement error in R. Lacking a means of measuring $\hat{b}_R$

in our data, we experimented with a range of values, including the experimentally determined value of 1.21 based on NanoString measurements by Li et al. We found that due to the relatively minor stochastic error in measurements of R, our estimates of $\hat{\sigma}^2_{\mathrm{PDT}}$ were robust to reasonable values of $\hat{b}_R$ (between 0.75 and 1.5) and so we elected to fix its value at 1. We then calculated variance explained as:

$$\frac{\hat{\sigma}^2_{\mathrm{MP}} - \hat{\sigma}^2_P - \hat{\sigma}^2_{\mathrm{PDT}}}{\hat{\sigma}^2_{\mathrm{MP}} - \hat{\sigma}^2_P}$$

We applied this equation both within each time point, and to the fold changes between each time point. Stochastic error terms for both within-stage and between stage values for R and P were calculated using limma and proDA respectively. Notably, correlation between the two sequencing assays and MS is strongly dependent on the magnitude of change at that time point, with technical noise specific to each assay non-correlated (Buccitelli and Selbach, 2020). For the R implementation of the above equations, see our github repository (https://github.com/ohlerlab/cortexomics), and the file src/Figures/Figure4/2_vardecomp.R.

Hierarchical clustering

For hierarchical clustering (**Table S3**), we took fold changes in RNA-seq and MS values relative to E12.5, for each gene, and carried out PCA on the resulting n x 8-dimensional matrix. We calculated Euclidean distances between genes and performed hierarchical clustering using the R function *hclust* and the 'ward' clustering criterion – i.e., favoring the creation of large clusters rather than small clusters containing few outliers. We found that our expression data showed a smooth reduction in variance explained as the number of clusters varied, and so we plotted GO-term enrichment for different cluster numbers, and finding that clusters with similar GO-term enrichments began to appear at a cluster number of 13 chose this as our cutoff. Meta-trajectories for each cluster were plotted using the median and upper/lower quartiles for each cluster. Enrichment of dTE genes in each cluster was calculated using Fisher's exact test (with dTE status, and inclusion in the cluster, as binary variables). GO term analysis of each cluster was carried out using topGO.

Nonlinear trajectory modeling

In order to model the nonlinear relationship between steady-state protein levels and Ribo-seq, a measure of protein synthesis, we used an approach similar to that used by (Becker et al., 2018) - our full '*production'* model represents the expression of each protein as the result of a synthesis rate, directly proportional to Ribo-seq footprint density with a proportionality constant Ks (or SDR - see (Riba et al., 2019)), and a decay rate Kd:

$$\frac{d(P)}{dt} = K^s R_g(t) - K^d P(t)$$

If the functional form of Ribo-seq density is modeled as a linear stepwise function, this equation has an analytic solution (Becker et al., 2018). In practice, the parameters Ks and Kd will be non-identifiable depending on the trajectory shape and half-life of the protein involved; for many proteins, only their ratio, defining the equilibrium steady state, can be estimated (along with the initial value of P). In addition to the '*production'* model, we included reduced versions of our model which fixed Kd at a high value (the '*linear'* model) giving a linear protein-Ribo-seq relationship, fixed Ks at a low value and modeled protein as controlled by degradation only (the *'degradation'* model), or fixed both to leave protein levels stationary (the *'stationary'* model). We further included a model allowing arbitrary deviations from the Ribo-seq trajectory (the *'MSdev'* model), since many proteins showed changes in their trajectory that were not explicable by any value of Ks and Kd. We used the bayesian information criterion (BIC) to select an optimal model for each gene, further requiring that residuals in this model be normally distributed (as per a chi-squared test). To estimate half-lives, we made the simplifying assumption of a single Ks value applying to all genes, allowing pi-half estimates to be derived for all proteins.

Stan files detailing the above models are available on the project github, and data are in **Table S3**.

Single cell RNA-seq data

Single cell RNA-seq (scRNA-seq) data in **Figure 3C** was derived from data and scripts in (Telley et al., 2019) and accompanying web resource:
http://genebrowser.unige.ch/telagirdon/#query_the_atlas.

1054 For each gene, it's occurrence in neocortex cells measured by scRNA-seq is presented as a
1055 heat map arranged by chronological time of cell collection (x-axis) vs. time since cell birth (y-
1056 axis), after a timed pulse with a FlashTag label *in utero*. These axes correspond to roughly
1057 orthogonal programs of gene expression change, with the y-axis describing differences
1058 between apical progenitors and differentiated neurons, and the x-axis describing differences
1059 between cells born at different stages of development.
1060

1061 **Sequence motif analysis**

1062 Motif analysis (**Figure 7A**) was performed with the AME program from the Meme suite as per
1063 (Becker et al., 2018; McLeay and Bailey, 2010) because we observed a systematic difference
1064 in UTR length between TE changing and TE unchanging genes. AME requires that input and
1065 control sequences are of approximately equal length distribution, so we created a sample of
1066 TE changing genes whose length distribution matched that of the TE unchanging genes. We
1067 ran AME with the CISBP-RNA database of RNA-binding protein motifs.
1068

1069 **Immuno-electron microscopy**

1070 Fixation, sectioning, immunolabeling, and electron microscopy were performed as described
1071 previously (Kraushar et al., 2021). E12.5 and E15.5 neocortex coronal sections were labeled
1072 with mouse anti-Rps5 (uS7; Santa Cruz, sc-390935) followed by 2.5 nm nanogold conjugated
1073 secondary antibody (Nanoprobes, 2001). Imaging was performed at 2700 x magnification on a
1074 Tecnai Spirit electron microscope. Quantification was performed in FIJI (Schindelin et al.,
1075 2012) with the Process > Find Maxima tool (as shown in **Figure 5C**, magenta pseudocolor),
1076 and Measure > Area tool, followed by statistical analysis in GraphPad Prism (GraphPad
1077 Software Inc.) to calculate puncta per μm^2 (Welch's ANOVA, Dunnett's *post hoc* test) (**Table**
1078 **S4**). Primary antibody leave-out controls were prepared in parallel, and were absent of
1079 nanogold signal (**Figure S5**).
1080

1081 **Expression vectors**

1082 For tdTomato reporter experiments, we used beta-actin driven expression constructs *pCAG-*
1083 *EGFP* and *pCAG-flox-STOP-flox-tdTomato*, as described previously (Ambrozkiewicz et al.,
1084 2017). A control vector with scrambled non-silencing shRNA (Ambrozkiewicz et al., 2018) was
1085 obtained from Thermo Scientific, and the shRNA to knock-down plasmid for mouse *eIF4EBP1*
1086 was obtained from Sigma Aldrich (TRCN0000335381).

1087

1088

1089 ***In utero* electroporation (IUE)**

1090 Mouse embryos were subjected to IUE exactly as described previously (Ambrozkiewicz et al.,
1091 2017, 2018, 2020). For the experiments with the tdTomato reporter in the Satb2$^{Cre/+}$ line, we
1092 used an equal amount of *pCAG-GFP* and *pCAG-flox-stop-flox-tdTomato*.

1093

1094 **Fluorescent *in situ* hybridization (FISH)**

1095 *In situ* hybridization using RNAscope Technology to detect mRNA of *Satb2* and *Bcl11b*
1096 (**Figures 3D and S4A**) was performed according to the manufacturer's protocols (ACD). Prior
1097 to hybridization, embryonic brains at E12.5, E14.5 and E16.5 were collected in PBS, fixed in
1098 4 % PFA/PBS prepared with DEPC for 16-20 hours at 4 °C. Brains were then incubated in
1099 sucrose solutions (10 % - 20 % - 30 %/PBS) until they reach osmotic equilibrium, embedded in
1100 O. C. T. Compound (Tissue-Tek) in a plastic cryoblock mold and frozen on dry ice. Coronal
1101 sections of 16 µm thickness were collected using a cryostat.

1102

1103 **Cryosectioning**

1104 For all histological procedures, brain sections were prepared on a Leica CM3050S cryostat.
1105 Prior to cryosectioning, brains were incubated for at least 5 hours with 10% sucrose in PBS,
1106 followed by incubation with 30% sucrose in PBS until the tissue reached osmotic equilibrium.
1107 Next, brains were frozen in -38 to -40°C isopentane (Roth). For processing of the tissue after *in*
1108 *utero* electroporation, coronal cryosections of 50 µm thickness were collected in PBS/0.01%
1109 sodium azide solution. For *in situ* hybridization and the mRNA/protein colocalization
1110 experiments (**Figures 3D and S4A**), 16 µm sections were collected.

1111

1112 **Immunohistochemistry**

1113 Fixed brain sections were washed with PBS three times at room temperature prior to the
1114 procedure to remove the sucrose and freezing compound residue. The sections were then
1115 incubated with Blocking solution (5% goat serum, 0.5% (v/v) Triton X-100, PBS) for one hour
1116 at room temperature, then with the primary antibody and DAPI diluted in blocking buffer for 16-
1117 20 hours at 4 °C, washed in PBS three times for 30 minutes and incubated with secondary
1118 antibody diluted in the blocking buffer for up to four hours at room temperature. Next, sections
1119 were incubated with PBS for 30 minutes three times and mounted with a cover glass (Menzel-

1120 Gläser) and Immu-Mount mounting medium (Shandon, Thermo-Scientific). For the experiment
1121 in **Figures 5D** and **S4A**, instead of mounting after the hybridization protocol, the sections were
1122 subjected to the immunohistochemistry as described here.
1123

1124 **Antibodies for immunohistochemistry**

1125 Primary antibodies used for immunocytochemistry were used at dilutions indicated: anti-Satb2
1126 (1:500, rabbit, home-made; (Ambrozkiewicz et al., 2017)), anti-Bcl11b (1:500, rat, Abcam,
1127 25B6, anti-Ctip2), anti-GFP (1:1000, goat, Rockland), anti-Cre (1:1000, rabbit, SySy), anti-Tbr2
1128 (1:300, rabbit, Abcam), anti-Pax6 (1:500, rabbit, Millipore), Draq5 (1:2000). All secondary
1129 antibodies were from Jackson Immunoresearch and were used at 1:250.
1130

1131 **Confocal imaging**

1132 Imaging of brain coronal cross sections after IUE was performed at the level of primary
1133 somatosensory cortex primordium. For imaging of the overview of immunostaining, a Leica
1134 SPL confocal microscope with 20X, 40X and 63X objectives was used. For quantitative
1135 imaging of FISH signal, a Leica Sp8 microscope with 40X objective was used. Quantification of
1136 mRNA cluster sizes, and mRNA and protein localization, was performed using ImageJ
1137 software.
1138

1139 **QUANTIFICATION AND STATISTICAL ANALYSIS**

1140 **Quantification of distribution and size of mRNA clusters**

1141 mRNA puncta were manually quantified using ImageJ software. The maximum intensity of
1142 confocal image Z-stacks was projected on a single 2D plane. After thresholding, the images
1143 were binarized using the watershed segmentation to separate cluster clouds. The number of
1144 particles of 0.1 μm^2 or bigger were then quantified using Measure Particles tool and
1145 normalized to the number of DAPI-labeled nuclei in a given cortical area (VZ, CP, etc.). Area of
1146 clusters was quantified as well and expressed as an absolute surface. See **Table S4.**
1147

1148 **Quantification of colocalization**

1149 Mander's colocalization coefficient was quantified for neurons expressing Satb2 and Bcl11b
1150 protein and mRNA. Protein colocalization was determined manually, and RNA colocalization
1151 was quantified using binarized images after multiplication. See **Table S4.**
1152

1153 **Quantification of neuronal cell markers**

1154 The manually quantified number of neurons expressing a given marker was normalized to the
1155 entire number of IUE-labeled neurons or to DAPI-labeled nuclei count. See **Table S4.**

1156

1157 **Statistical analyses**

1158 Statistics were performed using SPSS v.17 (San Diego, USA) or GraphPad Prism software. All
1159 numerical values and description of statistical tests used, definition of center, dispersion,
1160 precision, and definition of significance can be found in the **Table S4**. Prior to comparison of
1161 experimental groups, normality and log-normality test were performed.

1162

1163 **DATA AVAILABILITY**

1164 Code generated during this study is supplied at: https://github.com/ohlerlab/cortexomics.

1165 RNA-seq data are publicly available in the NIH GEO: GSE157425.

1166 Ribo-seq data are deposited in the NIH GEO: GSE169457.

1167 tRNA qPCR array data are deposited in the NIH GEO: GSE169621.

1168 Mass spectrometry data are publicly available in the ProteomeXchange: PXD014841.

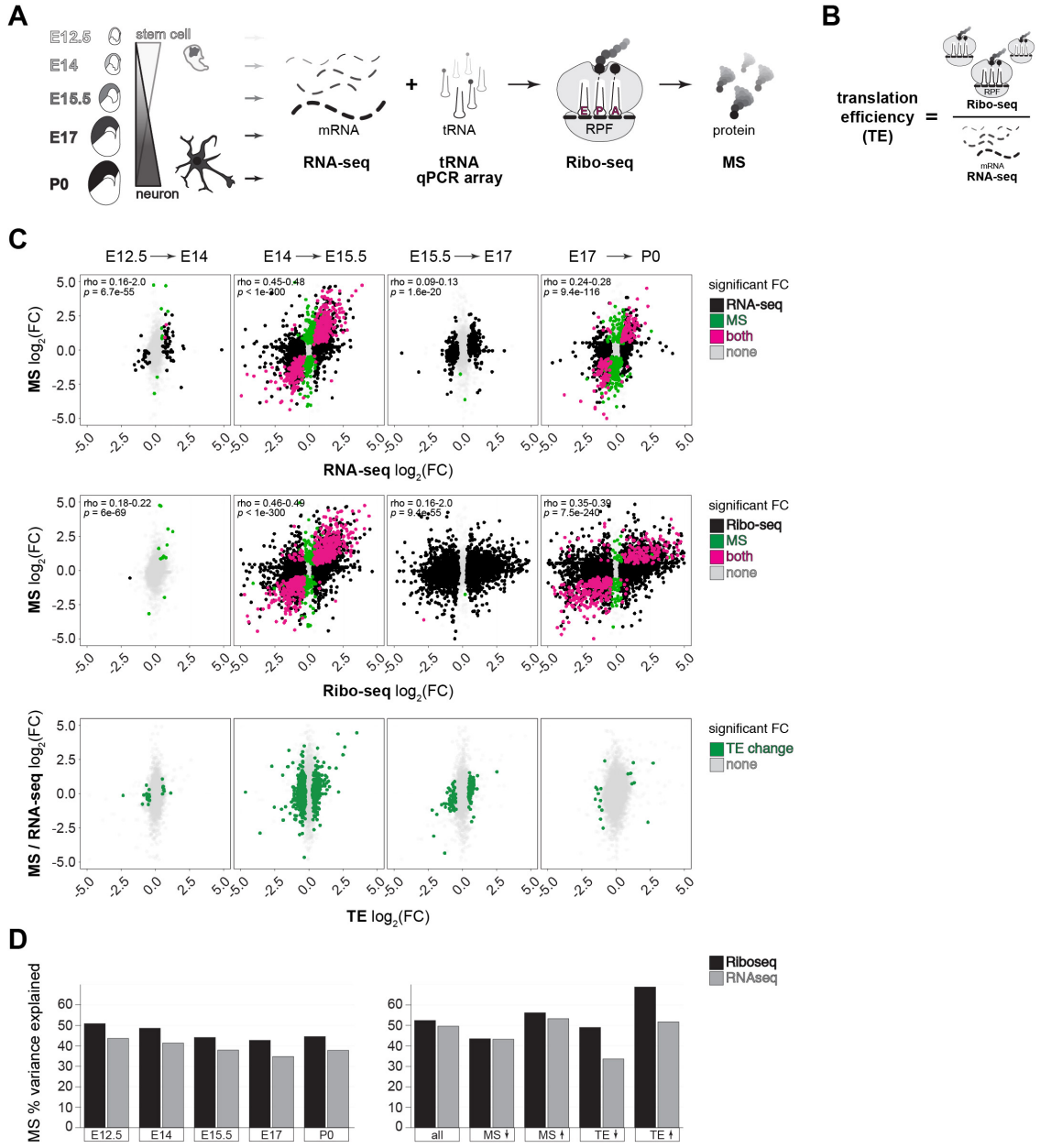

Figure 1. A transient spike in translation regulation occurs at mid-neurogenesis during prenatal development. **(A)** Neural stem cell differentiation in the brain's neocortex, analyzed by RNA-seq, Ribo-seq, tRNA qPCR array, and MS at embryonic (E12.5-E17) and postnatal (P0) stages. **(B)** Schematic of translation efficiency (TE). **(C)** Sequential fold changes in post-transcriptional gene expression between adjacent stages, comparing mRNA vs. protein (top), mRNA translation vs. protein (middle), and calculated translation efficiency (bottom). Significance assessed at ≥ 1.25 FC, $p < 0.05$. **(D)** The percent variance in MS explained by RNA-seq or Ribo-seq at each developmental stage, and for subgroups with MS and translation efficiency changes. See also **Figures S1-S3A** and **Tables S1-2**.

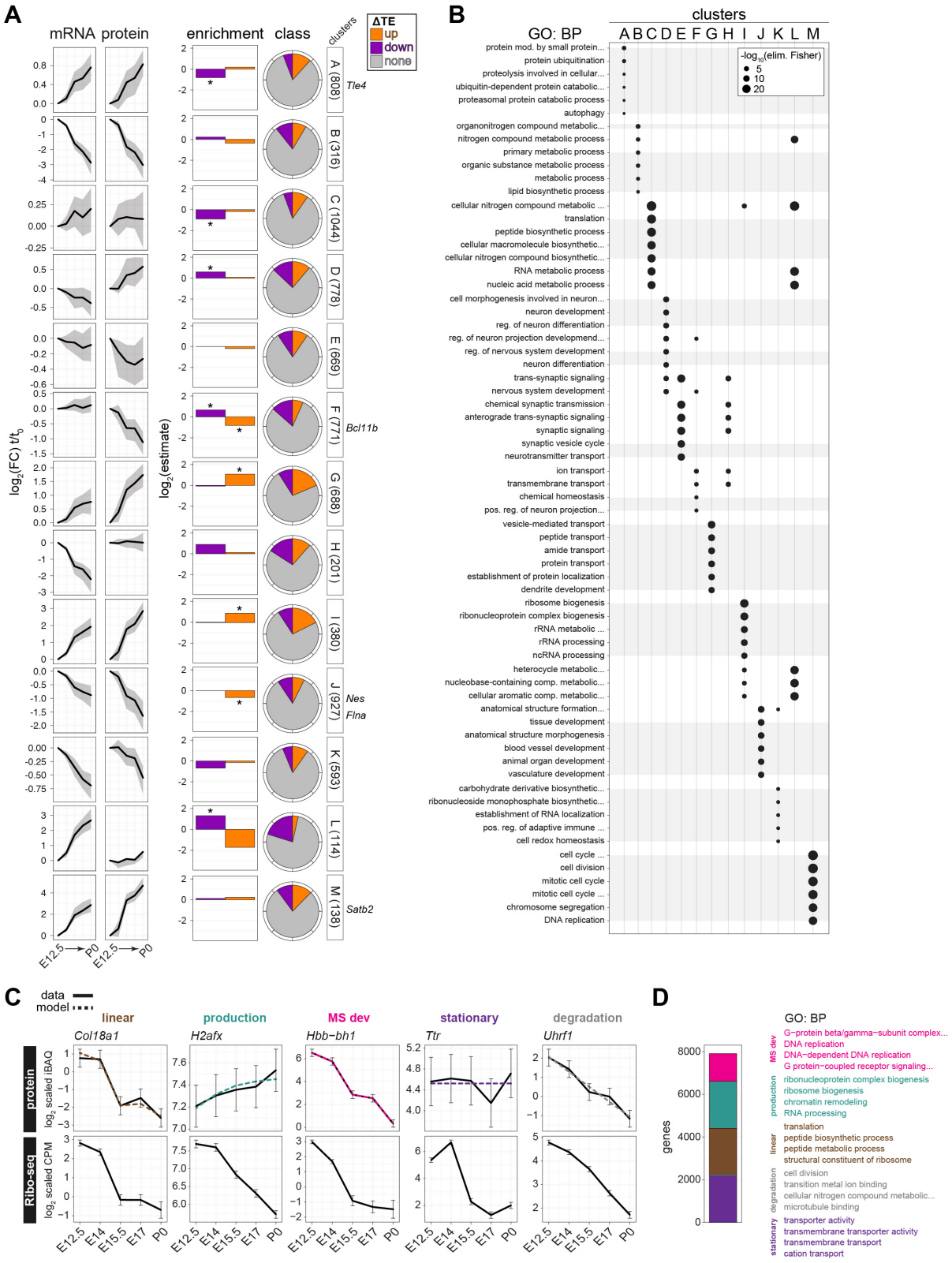

Figure 2. Modeling divergent trajectories of mRNA and protein expression by translation regulation.
(A) mRNA (RNA-seq) and protein (MS) expression per gene from E12.5 (t_0) to subsequent stages (t) clustered by trajectory. The median trajectory is shown, with upper and lower quartiles (grey). Enrichment and proportion of TE up and down genes in each cluster, with significant enrichment (*$p < 0.05$). Example neural stem cell and neuronal marker genes are indicated (right). **(B)** Gene ontology (GO, biological process) enrichment for each cluster, with unique terms for a cluster outlined in grey. **(C)** Modeling of non-linear relationships between Ribo-seq and MS comparing active translation vs. steady-state protein, with representative genes shown for each category. See text for details. **(D)** Proportion of total genes in each category from (C), with enriched GO terms per category. Fisher's exact test, $p < 0.05$. See also **Figure S3B-D** and **Table S3**.

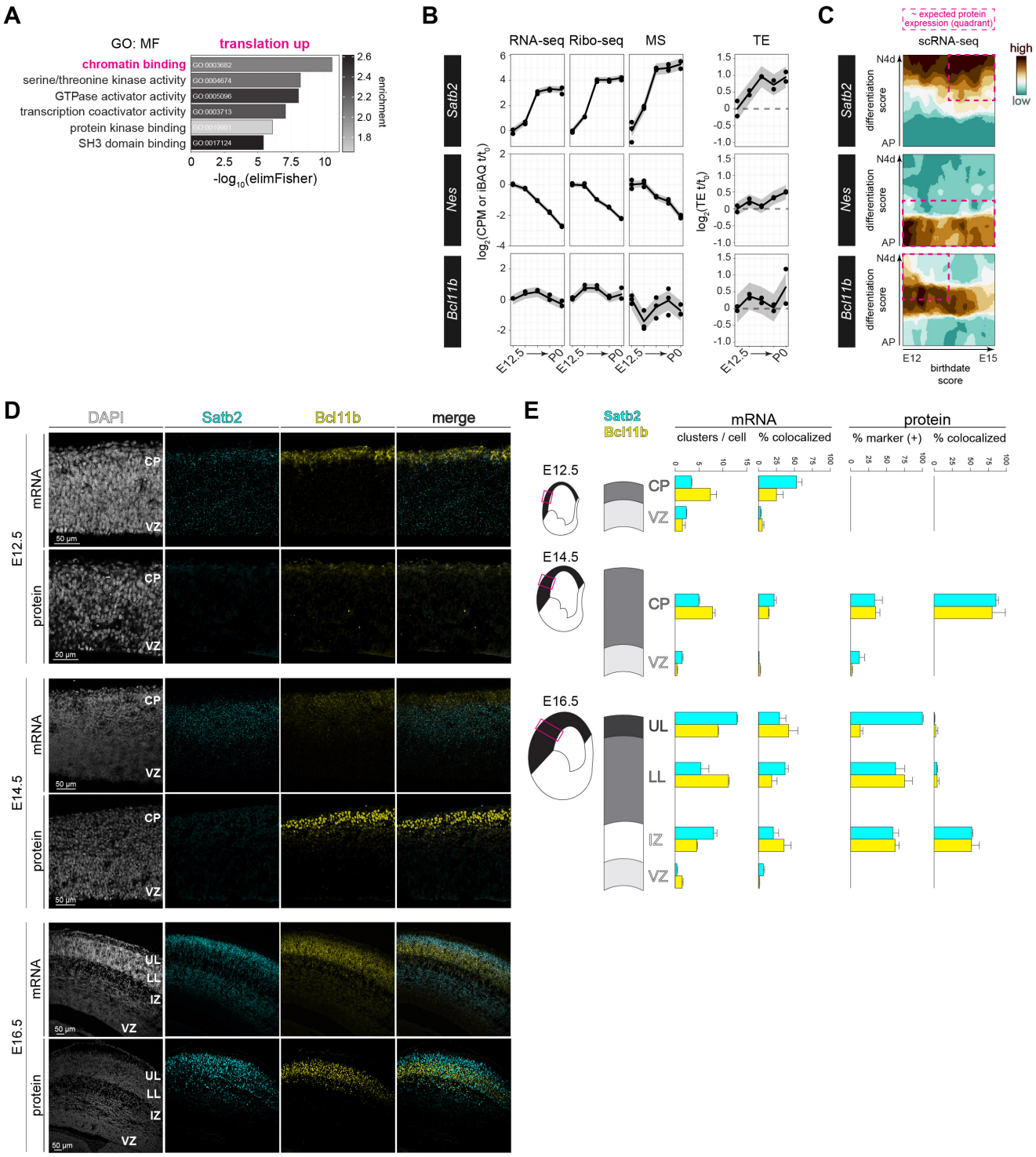

Figure 3. Translation upregulation of *Satb2* leads to divergent spatiotemporal mRNA and protein expression. **(A)** Gene ontology (GO, molecular function) analysis of translationally up-regulated (TE up) mRNAs. **(B)** The trajectory of *Satb2, Nes,* and *Bcl11b* gene expression measured by RNA-seq, Ribo-seq, MS, and translation efficiency. **(C)** *Satb2, Nes,* and *Bcl11b* expression in scRNA-seq data tracking differentiating neocortex cells at 1, 24, or 96 hours after birth (y-axis), at birthdates E12, E13, E14, or E15 (x-axis) (Telley et al., 2019). Expected distribution of protein expression (DeBoer et al., 2013) is outlined. **(D)** Neocortex coronal sections at E12.5, E14.5, and E16.5 analyzed for *Satb2* and *Bcl11b* mRNA by fluorescence *in situ* hybridization, and protein by immunohistochemistry. DAPI (nuclei). Ventricular zone (VZ), cortical plate (CP), lower layers (LL), upper layers (UL). **(E)** Quantification of (D). Mean ± SEM. See also **Figure S4A-B** and **Table S4**.

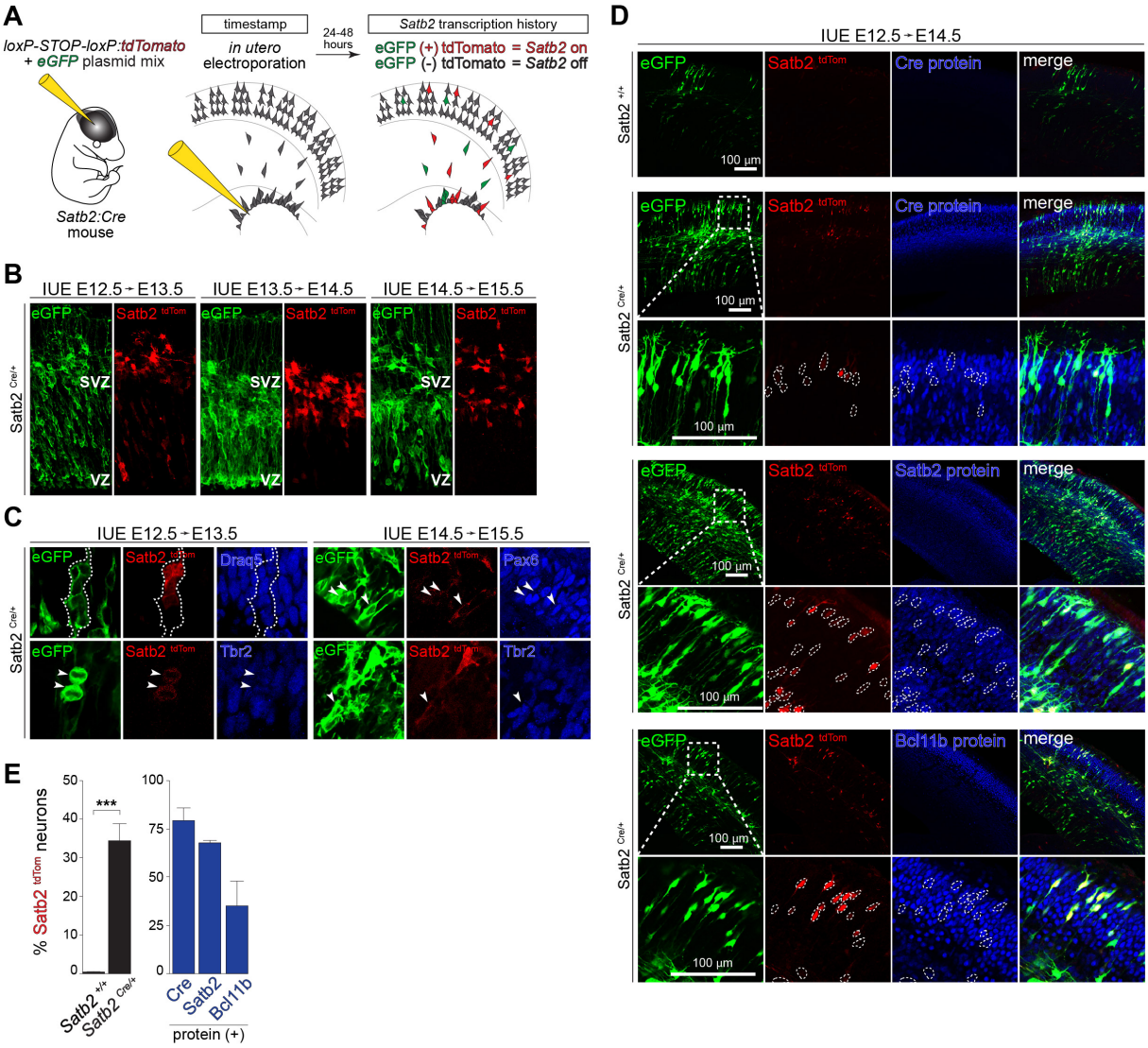

Figure 4. *Satb2* transcription is activated unexpectedly broadly and early in neural stem cell lineages.
(A) Schematic of the experimental approach. **(B)** *Satb2* transcription activity visualized by Cre-driven (*Satb2*$^{Cre/+}$) tdTomato expression, with reporter *in utero* electroporation (IUE) at E12.5, E13.5, or E14.5 and imaged after 24 hours. Co-electroporation of an eGFP plasmid labels all transfected cells. Ventricular zone (VZ), subventricular zone (SVZ). **(C)** *Satb2*^{tdTom} co-immunolabeling with Pax6 (apical progenitors), Tbr2 (intermediate progenitors), and Draq5 (nuclei). **(D)** *Satb2*^{tdTom} expression at E12.5-E14.5, with co-immunolabeling for neuronal fate determinant proteins Satb2 and Bcl11b, among all electroporated cells (eGFP). Negative control is the absence of *Cre* (Satb2$^{+/+}$). **(E)** Quantification of (D) for the expression of Cre, Satb2, and Bcl11b proteins in cells transcribing *Satb2* mRNA (*Satb2*^{tdTom}). Mean ± SD, unpaired t-test, ***$p < 0.0001$. See also **Figure S4C** and **Table S4**.

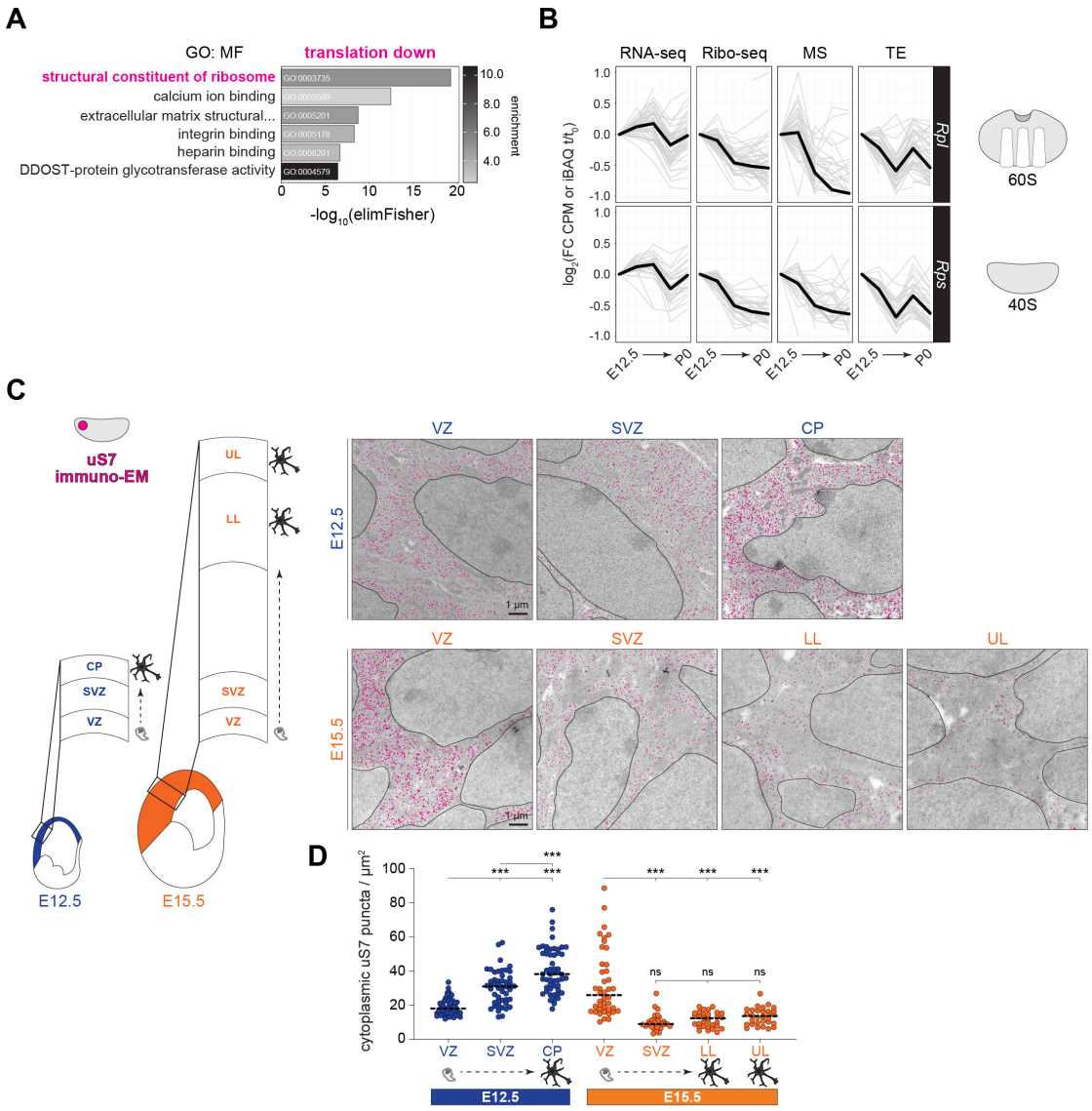

Figure 5. Translation downregulation decreases ribosome levels acutely at mid-neurogenesis.
(A) Gene ontology (GO, molecular function) analysis of translationally down-regulated (TE down) mRNAs. **(B)** The expression trajectories (grey) of all 79 ribosomal protein coding mRNAs in the large (*Rpl*) and small (*Rps*) subunits from E12.5 (t_0) to subsequent stages (t), measured by RNA-seq, Ribo-seq, MS, and calculated translation efficiency. Median trajectories are shown (black). **(C)** Immuno-electron microscopy labeling ribosomal protein uS7 (magenta) in the E12.5 and E15.5 neocortex neural stem cells and neurons, with **(D)** quantification for ribosomes per cytoplasmic area. Mean shown (line), Welch's ANOVA and Dunnett's *post hoc* test, ***$p < 0.001$. Neural stem cells are located in the ventricular zone (VZ) and sub-ventricular zone (SVZ); post-mitotic neurons are located in the cortical plate (CP), lower layers (LL), upper layers (UL). Nuclei are outlined. See also **Figure S5** and **Table S4**.

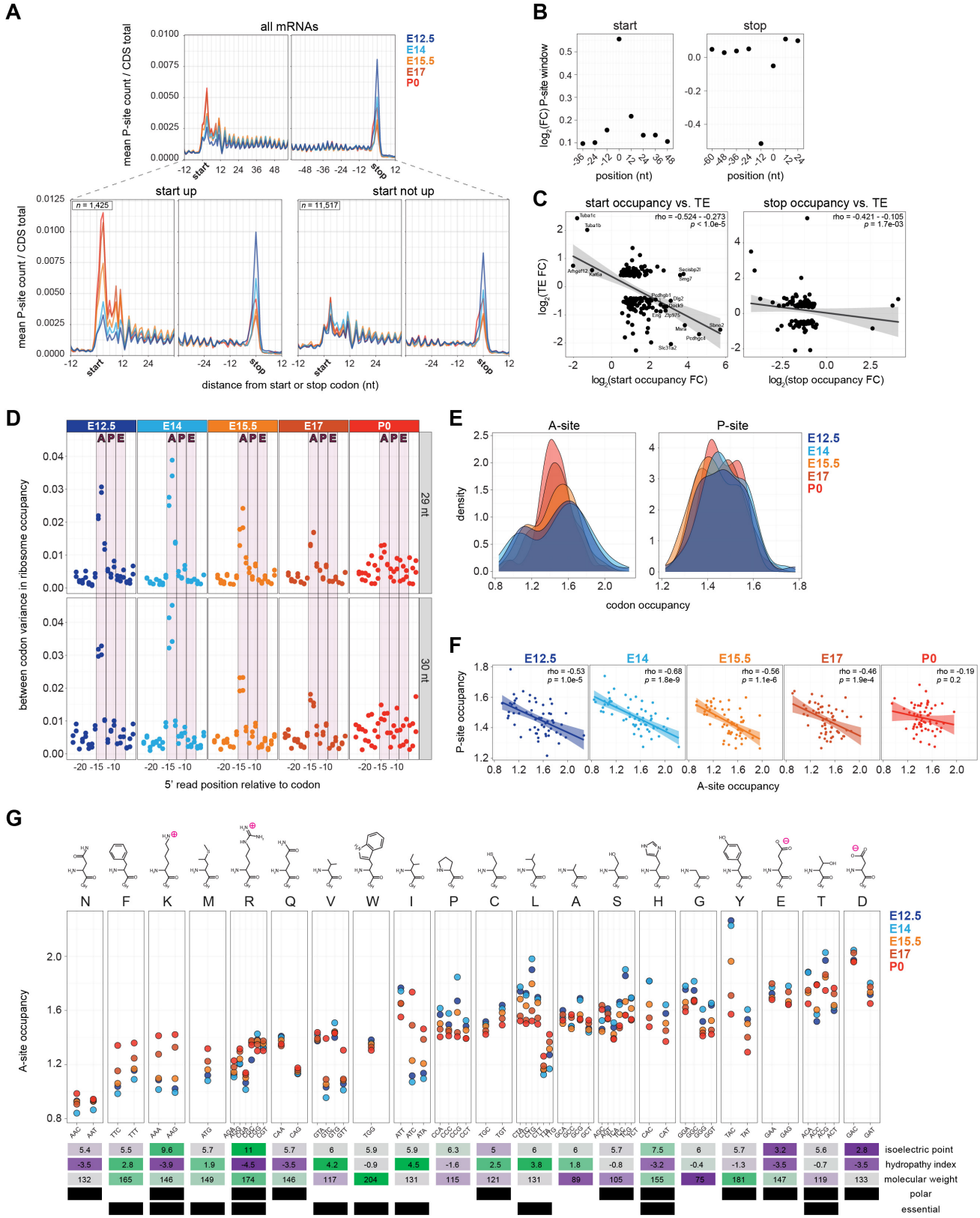

Figure 6. Ribosome density at the start codon and in the CDS shifts sharply at mid-neurogenesis.
(A) Ribosome occupancy metagene plot including all mRNAs (top) surrounding the start (left) and stop (right) codons at five stages. Separation of mRNAs by changing or unchanged start codon occupancy (bottom). **(B)** Position specific fold changes in ribosome P-site counts surrounding the start and stop codons. **(C)** Start (left) and stop (right) codon occupancy vs. TE fold change per gene. **(D)** Between codon variance in ribosome occupancy of A-, P-, and E-sites at each stage. Calculation with both 29 nt (top) and 30 nt (bottom) RPF fragments shown. **(E)** Distribution of per-codon ribosome A- and P-occupancy at each stage. **(F)** Correlation between A- and P-site occupancy per codon. **(G)** Ribosome A-site occupancy for each amino acid with corresponding synonymous codons at each stage. See also **Figures S6-S7** and **Table S5**.

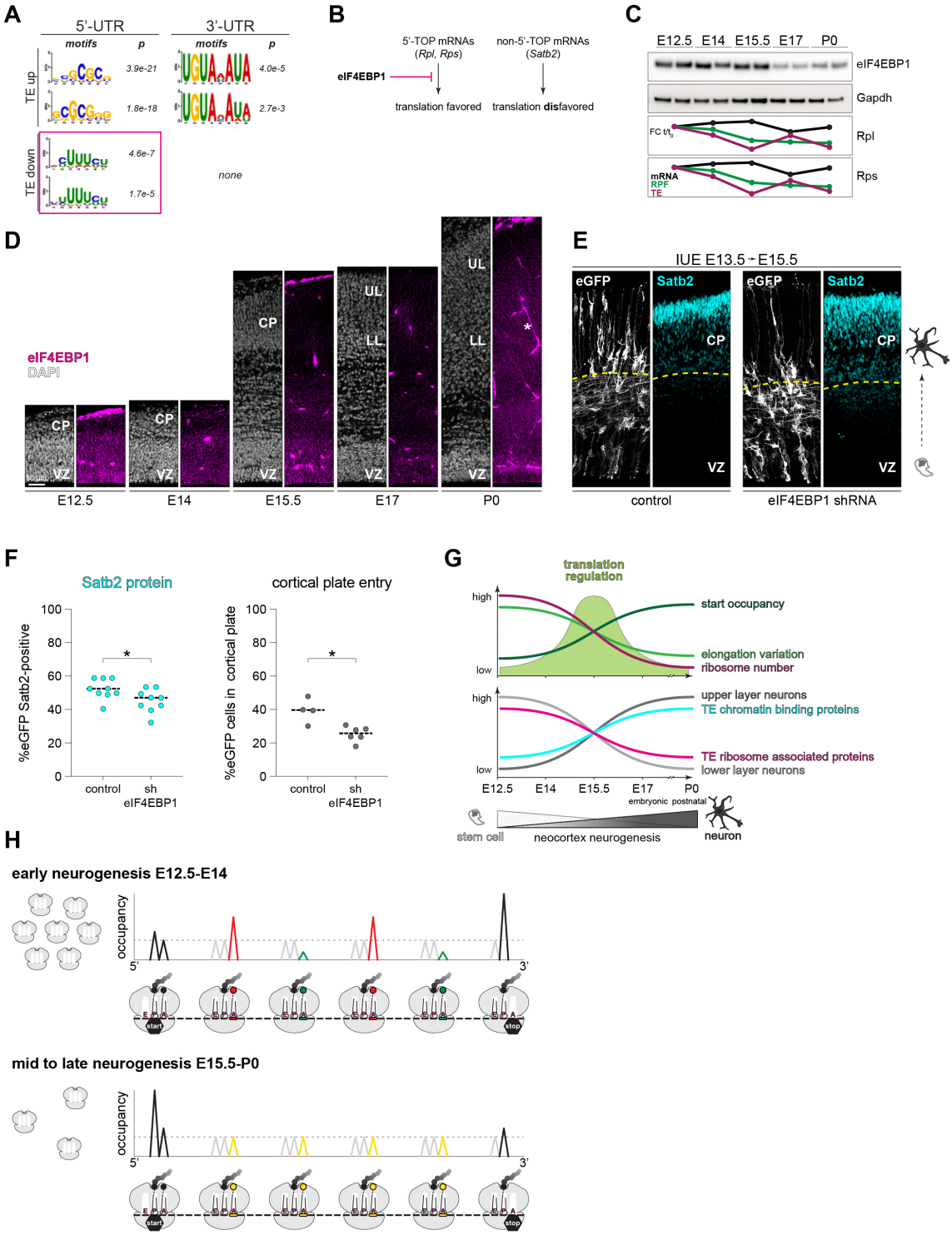

Figure 7. eIF4EBP1 levels coincide with ribosome abundance and control neuronal Satb2 fate *in vivo*.
(A) Positional weight matrix of the top two motifs ranked by *p*-value in the 5' and 3'-UTRs of TE up or down mRNAs. 5' terminal oligopyrimidine (TOP) motifs are highlighted for TE down genes. **(B)** eIF4EBP1 inhibition of ribosomal protein coding mRNA 5'-TOP sequence translation. **(C)** Western blot analysis of eIF4EBP1 levels in neocortex lysates in biological duplicate (n = 4-6 neocortex hemispheres per lane). Concurrent trajectory of Rpl and Rps translation shown below. **(D)** Immunohistochemistry analysis of eIF4EBP1 expression in neocortex coronal sections across neurogenesis. Blood vessels (star) are a common staining artifact. **(E)** shRNA knockdown of eIF4EBP1 compared to scrambled control by *in utero* electroporation (IUE) at E13.5 followed by analysis at E15.5 with Satb2 protein immunolabeling. Co-electroporation of eGFP labels all transfected cells. Cortical plate neuron boundary is demarcated (dotted line). **(F)** Quantification of (E) per animal for the percent of electroporated cells expressing Satb2 protein (left), and number of cells migrating into the cortical plate (right). Median (line), Mann-Whitney test, $*p < 0.05$. **(G)** Summary of timed translation changes and neuronal specification during neocortex development. **(H)** Model of early vs. late neurogenesis ribosome levels and per-codon changes in ribosome occupancy. See also **Table S4**.

Supplemental Information

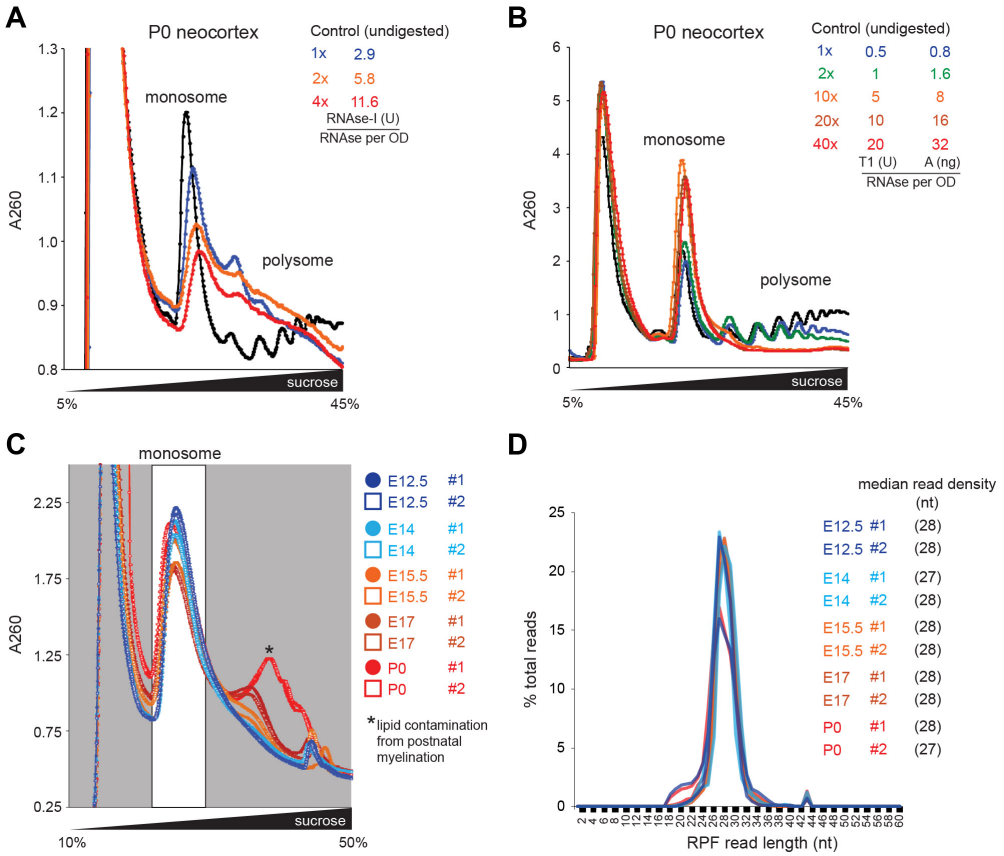

Figure S1. Optimized ribosome protected mRNA fragment purification from neocortex.
Nuclease digestion for the generation of ribosome protected mRNA fragments (RPFs) from P0 neocortex, with **(A)** RNAse-I vs. **(B)** a combination of RNAse-T1 & A. Absorbance at 260 nm (A260). Chains of actively translating ribosomes (polysome) should be digested into single ribosomes (monosome). RNAse-I, typically used in yeast, was inefficient in neocortex lysates, and thus an RNAse-T1 & A protocol was used for this study. **(C)** Nuclease digestion and purification of neocortex RPFs in biological duplicates at each developmental stage with the optimized protocol from (B). Each biological replicate included 17-40 brains (34-80 neocortex hemispheres) as detailed in the **Methods**. **(D)** RPF read length distribution. Associated with **Figure 1**. See also **Table S1**.

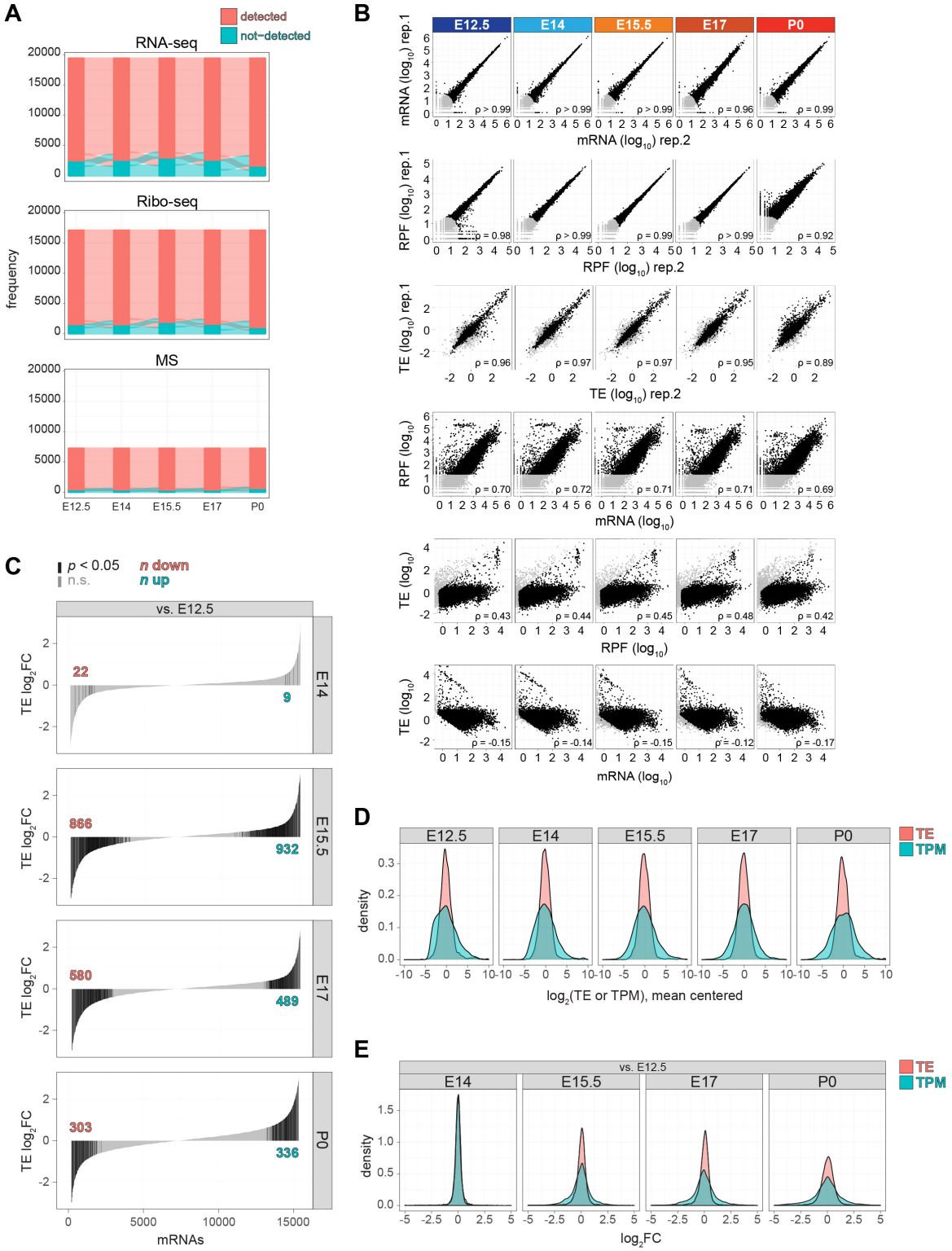

Figure S2. Neocortex RNA-seq, Ribo-seq, MS, and translation efficiency data characteristics.
(A) River plots demonstrating the number of unique genes detected across all 5 stages measured by RNA-seq, Ribo-seq, or mass spectrometry, compared to the number detected in <5 stages. **(B)** Biological replicates of transcripts per million (TPM) measured by RNA-seq (mRNA), Ribo-seq (RPF), and calculated translation efficiency (TE), including correlations between RPF and TE with mRNA to highlight genes with robust translation regulation. **(C)** The distribution of TE up and down fold changes (FC) compared to the earliest stage E12.5, with significant genes highlighted in black ($p < 0.05$). **(D)** The distribution of TE and mRNA abundance (TPM) for all genes at each stage, and **(E)** fold changes vs. the earliest stage E12.5. Associated with **Figure 1**. See also **Tables S1-2**.

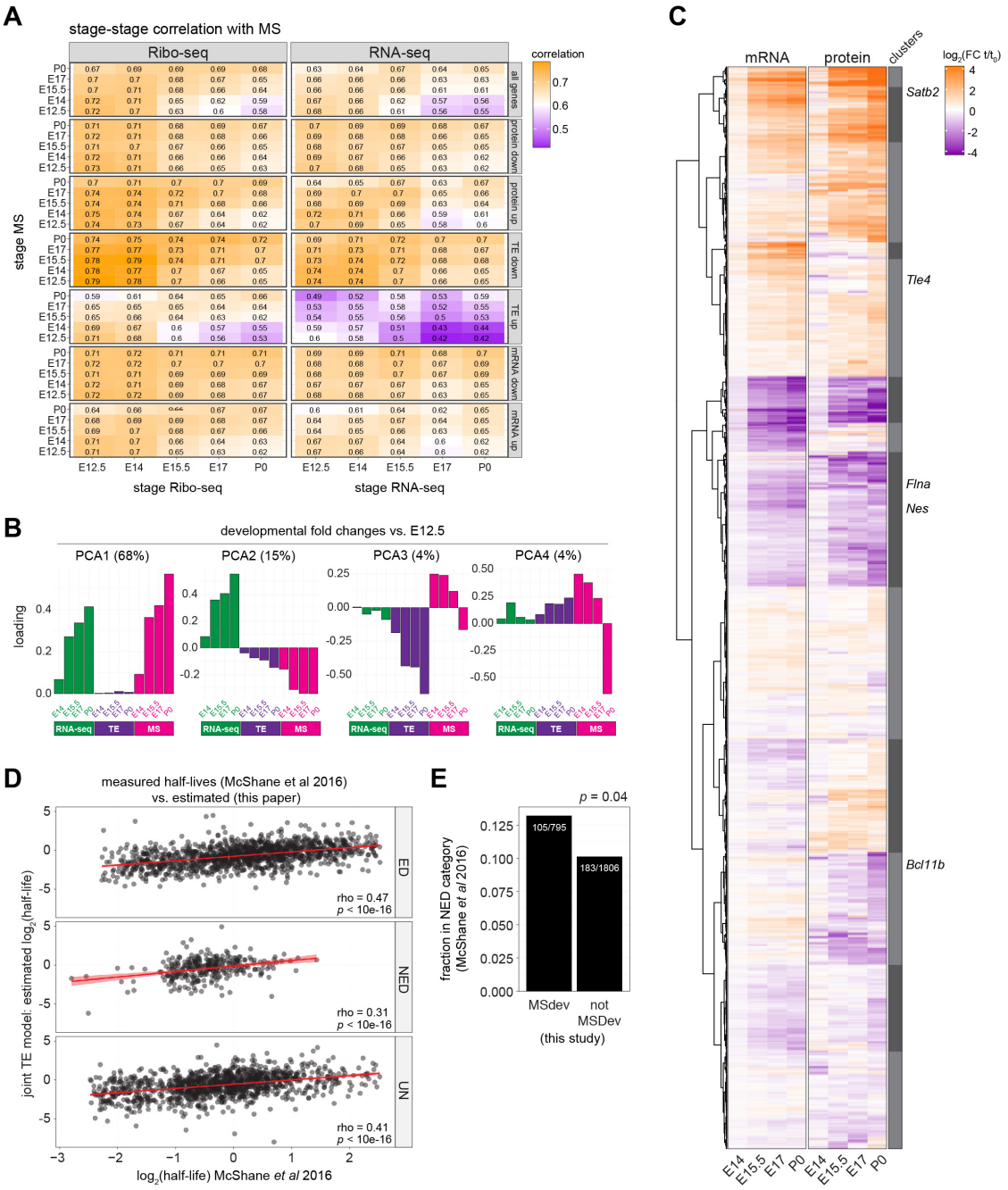

Figure S3. Modeling of mRNA translation.
(A) Correlation between MS and Ribo-seq or RNA-seq for all genes, and those with changing protein, TE, and mRNA levels. **(B)** Principal component analysis (PCA) of developmental fold changes in RNA-seq, TE, and MS compared to the earliest stage E12.5. The first four components are shown, with percent variance annotated. **(C)** Hierarchical clustering based on mRNA (RNA-seq) and protein (MS) expression trajectories per gene. Fold change expression increasing or decreasing from E12.5 (t_0) to subsequent developmental stages (t) shown in heat map. Neural stem cell and neuronal marker genes are indicated (right). **(D)** Protein half-lives measured by SILAC MS and categorized as exponential decay (ED), non-exponential decay (NED), or neither (UN) in (McShane et al., 2016) correlated with the model estimates from our data as per (Becker et al., 2018). **(E)** The fraction of genes modeled as MS deviating or non-deviating in this study that are categorized as NED proteins in (McShane et al., 2016). Associated with **Figure 2**. See also **Table S3**.

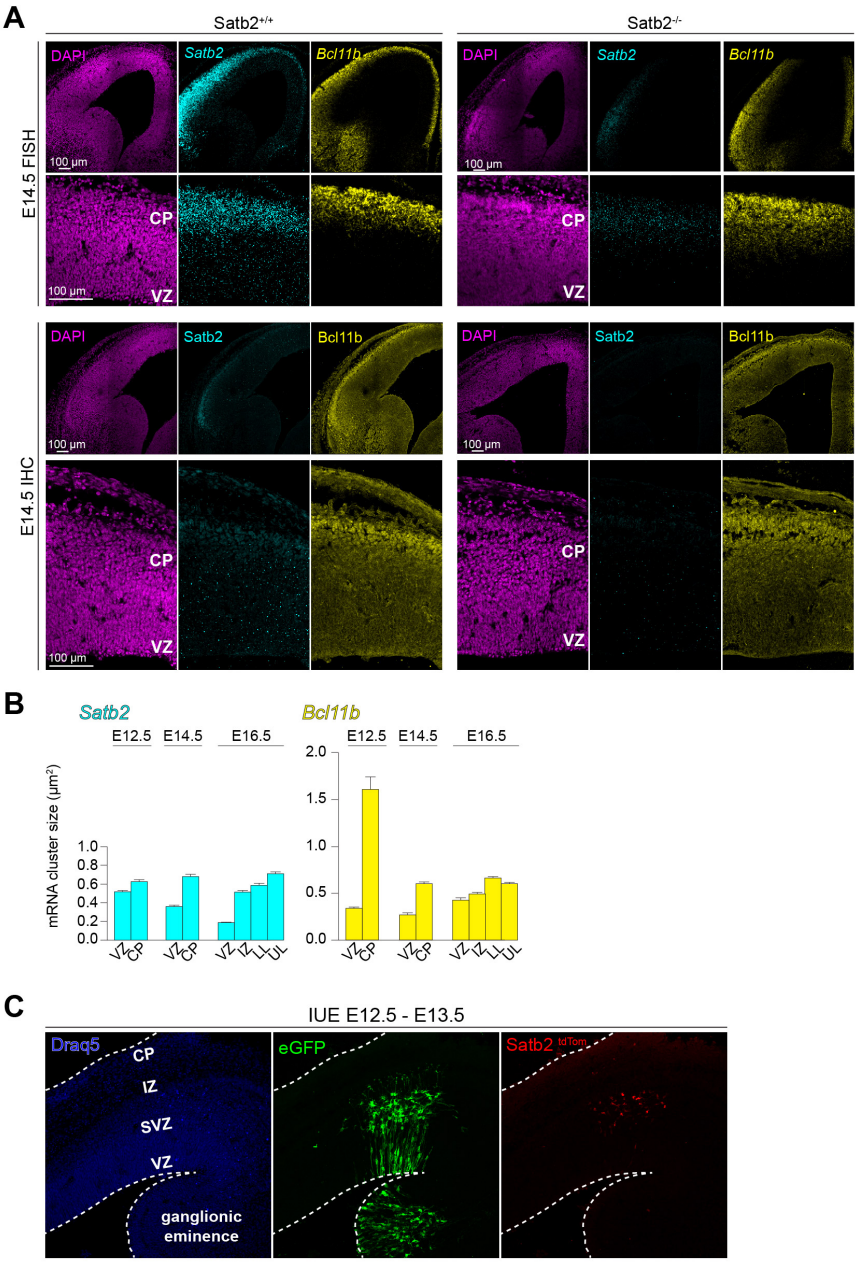

Figure S4. *Satb2*$^{-/-}$ control for FISH and IHC and neocortex-specific *Satb2* transcription.
(A) Fluorescence *in situ* hybridization (FISH) and immunohistochemistry (IHC) probing for *Satb2* and *Bcl11b* mRNA and protein, respectively, in wild-type (*Satb2*$^{+/+}$) and *Satb2* knockout (*Satb2*$^{-/-}$) neocortex coronal sections at E14.5. Ventricular zone (VZ), cortical plate (CP). **(B)** Measurement of *Satb2* and *Bcl11b* mRNA cluster sizes in FISH probed neocortex sections at three developmental stages. Intermediate zone (IZ), lower layers (LL), upper layers (UL). Mean ± SEM. **(C)** *Satb2* transcription activation visualized in *Satb2*$^{Cre/+}$ mice by *in utero* co-electroporation of the neocortex and ganglionic eminence with a *loxP-STOP-loxP-tdTomato* (*Satb2*^{tdTom}) fluorescence reporter at E12.5, along with eGFP reporter for all transfected cells, and analysis in coronal sections at E13.5. Sub-ventricular zone (SVZ). Associated with **Figures 3-4**. See also **Table S5**.

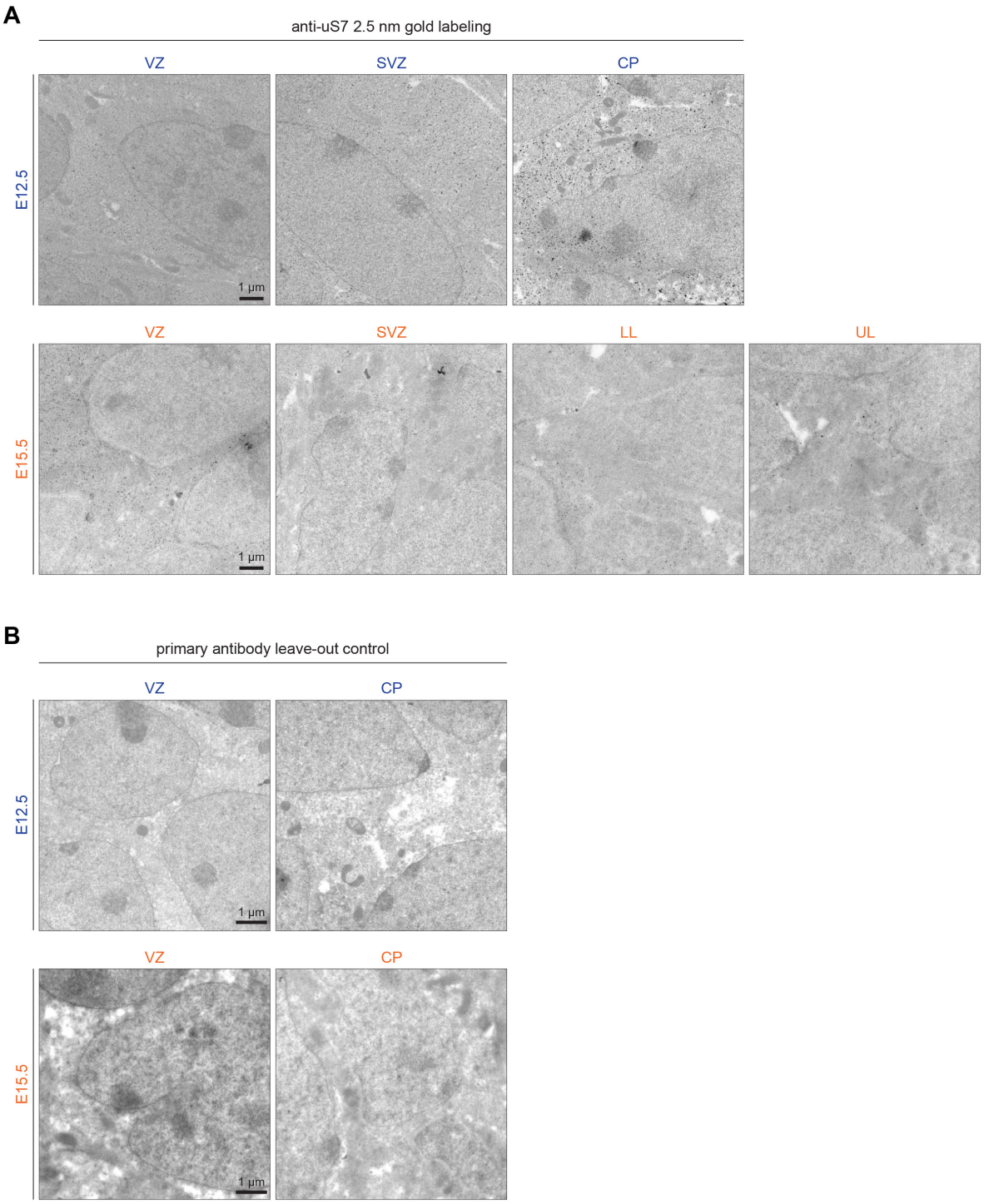

Figure S5. Immuno-electron microscopy labeling of ribosomes.
(A) Raw images of neocortex coronal sections at E12.5 and E15.5 shown in **Figure 5C**, immunolabeled with anti-ribosomal protein uS7 followed by 2.5 nm gold secondary (dark black spots), which were automatically detected and quantified in FIJI (magenta spots in **Figure 5C**). Electron microscopy was performed in regions corresponding to the stem cell niches of the ventricular zone (VZ) and sub-ventricular zone (SVZ), in addition to regions of differentiating neurons in the cortical plate (CP), which includes both lower layers (LL) and upper layers (UL) at later stages. Quantification of nanogold secondary signal was performed per unit area of the cytoplasm, with nuclei excluded by tracing the nuclear membrane (black lines in **Figure 5C**). **(B)** Primary antibody leave-out controls were prepared in parallel.

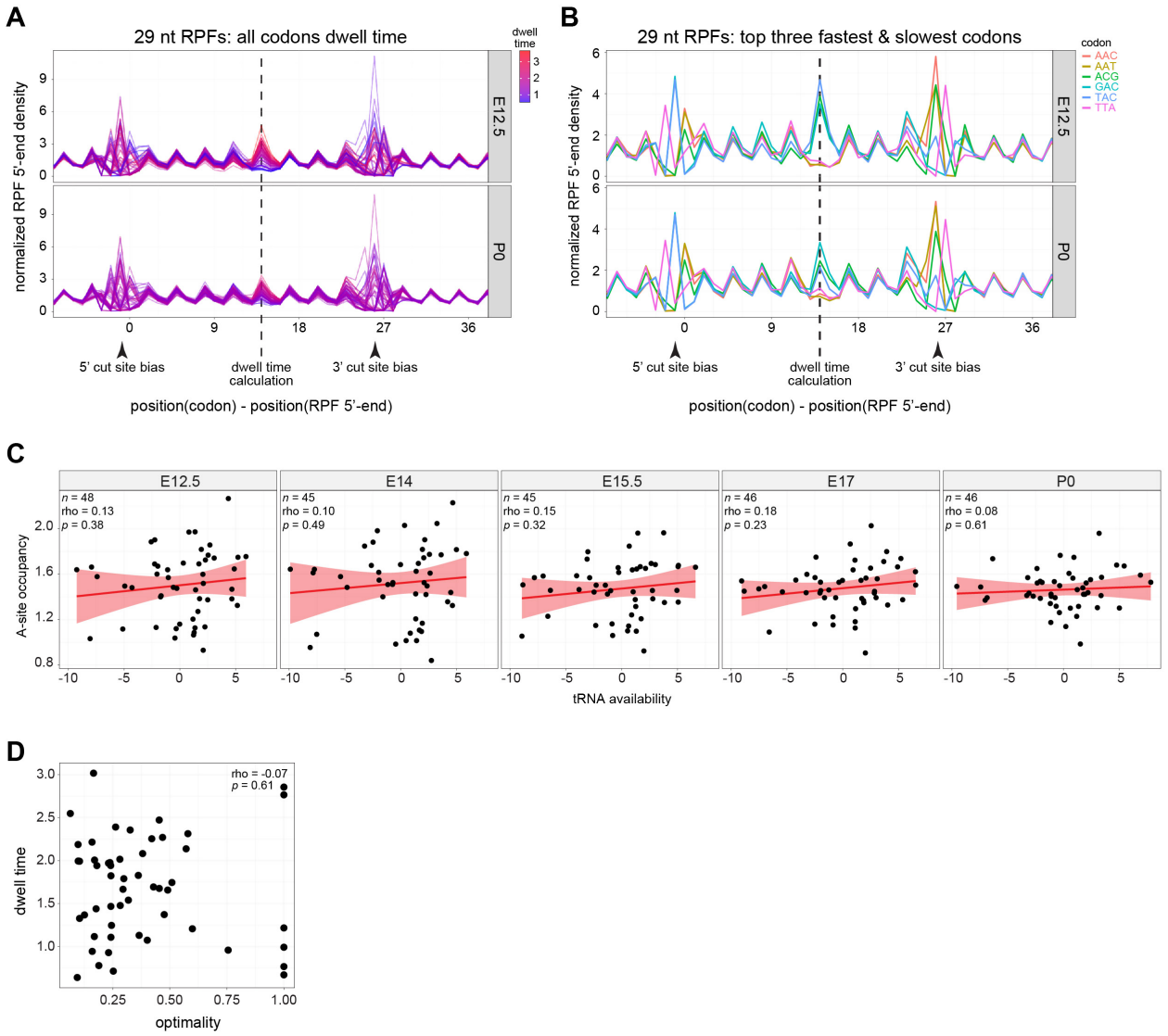

Figure S6. Analysis of per-codon ribosome density.
5' normalized ribosome-protected mRNA fragment (RPF) density for **(A)** all codons and **(B)** the top 3 slowest/fastest codons. Plotting the normalized density of Ribo-seq read 5' ends relative to each codon/read length/sample shows two strongly variable regions corresponding to 5'- and 3'-end cut site biases during nuclease digestion. A third variable region in between corresponds to RPFs with their A/P-sites positioned over the codon. We infer the location of the A-site as the 3 bp region showing the most inter-codon variability, and use the normalized occupancy here to measure codon dwell times, and variance between codons. Independently, this region also identifies the location of intra-codon variability between samples. **(C)** Per-codon correlation between tRNA availability calculated from tRNA qPCR array (see **Methods**), and the ribosome occupancy of that codon when positioned in the A- or P-site of the ribosome footprint. **(D)** Correlation between ribosome dwell time per codon and the optimality of the codon as defined in (dos Reis et al., 2004), with the mean across all stages shown. Associated with **Figure 6**. See also **Table S5**.

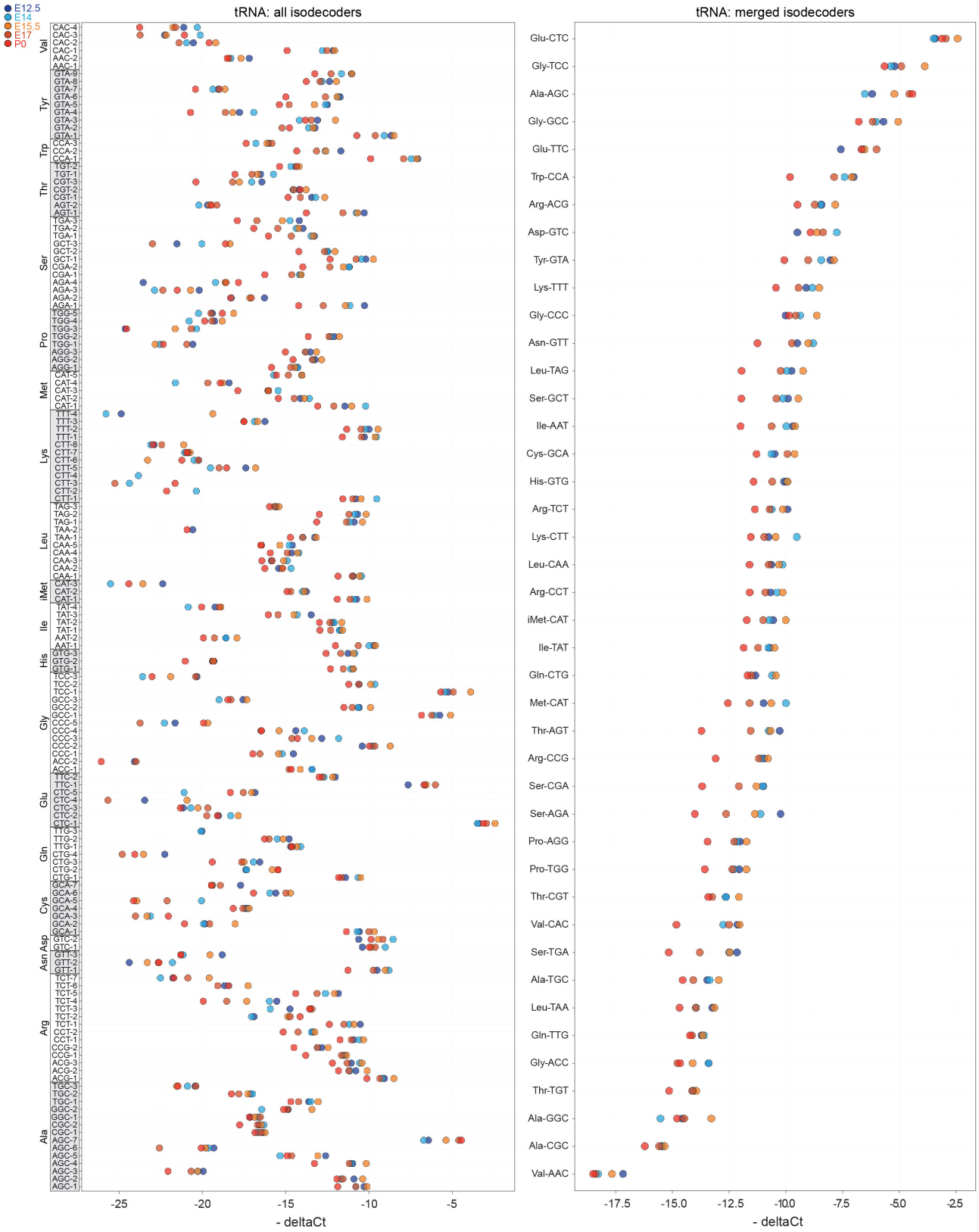

Figure S7. Neocortex tRNA qPCR array.
Total tRNA levels at each stage measured by qPCR array in biological duplicate, with Ct values for each tRNA isodecoder (left) or averaged across isodecoders (right) compared to the mean of 5S and 18S rRNA levels in each sample (delta Ct). Associated with **Figure 6**. See also **Table S5**.

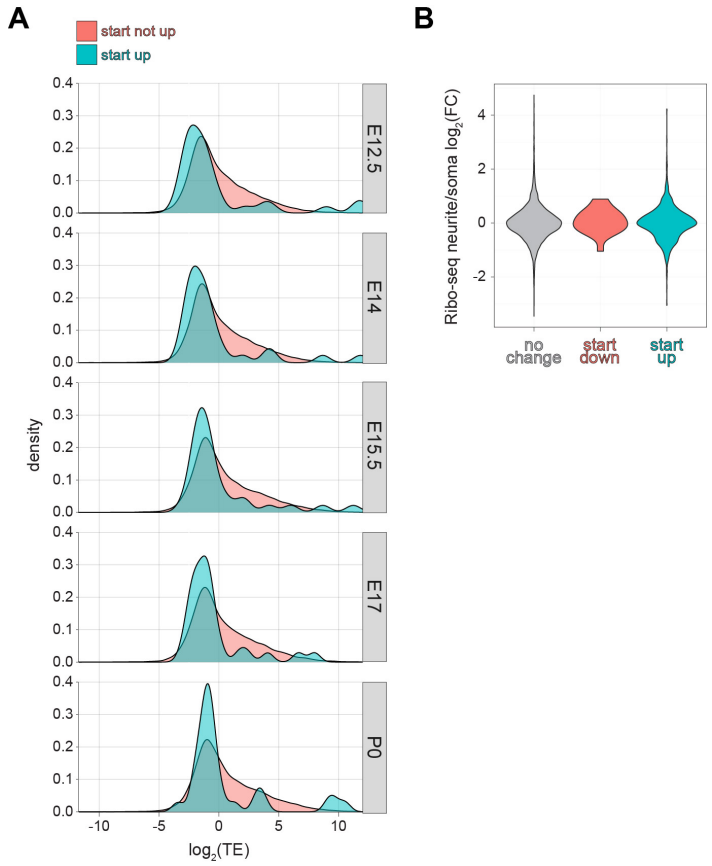

Figure S8. Start codon effect analysis.
(A) TE distribution for genes with increasing start codon occupancy across developmental stages, compared to those without start occupancy changes. **(B)** The association of mRNAs demonstrating start codon occupancy changes with translation in neurites vs. the soma of cultured neurons (Zappulo et al., 2017). Associated with **Figure 6**.